



# New smart twisting active rotor (STAR): pretest predictions

Berend G. van der Wall<sup>1</sup> · Joon W. Lim<sup>2</sup> · Johannes Riemenschneider<sup>1</sup> · Steffen Kalow<sup>1</sup> · Gunther A. Wilke<sup>1</sup> · D. Douglas Boyd Jr.<sup>3</sup> · Joelle Bailly<sup>4</sup> · Yves Delrieux<sup>4</sup> · Italo Cafarelli<sup>4</sup> · Yasutada Tanabe<sup>5</sup> · Hideaki Sugawara<sup>5</sup> · Sung N. Jung<sup>6</sup> · Seong H. Hong<sup>6</sup> · Do-Hyung Kim<sup>7</sup> · Hee J. Kang<sup>7</sup> · George Barakos<sup>8</sup> · Rinaldo Steininger<sup>8</sup>

Received: 19 February 2024 / Revised: 19 February 2024 / Accepted: 28 February 2024  
© The Author(s) 2024

## Abstract

A Mach-scaled model rotor with an active twist capability is in preparation for a wind tunnel test in the large low-speed facility of the German-Dutch wind tunnel (DNW) with international participation by the German Aerospace Center (DLR), US Army Combat Capabilities Development Command (DEVCOM) Aviation & Missile Center, National Aeronautics and Space Administration, French Aerospace Lab (ONERA), Korea Aerospace Research Institute, Konkuk University, Japan Aerospace Exploration Agency, Glasgow University, and DNW. To get the maximum benefit from the test and the most valuable data within the available test time, the tentative test matrix was covered by predictions of the partners, active twist benefits were evaluated, and support was provided to the test team to focus on the key operational conditions.

**Keywords** Active twist · Active rotor blade control · Blade–vortex interaction (BVI) noise · Helicopter vibration · Rotor stall · High advance ratio · Slowed rotor concept

## List of symbols

$A$  Rotor disk area =  $\pi R^2$ , m<sup>2</sup>  
 $c$  Rotor blade chord length, m

$C_{c,c,m}$  Blade element chordwise, normal force, and moment coefficient  
 $C_{L,X}$  Rotor lift and drag coefficients  
 $C_p$  Power coefficient =  $P/(\rho A[\Omega R]^3)$

✉ Berend G. van der Wall  
berend.vanderwall@dlr.de

Johannes Riemenschneider  
johannes.riemenschneider@dlr.de

Steffen Kalow  
steffen.kalow@dlr.de

Gunther A. Wilke  
gunther.wilke@dlr.de

D. Douglas Boyd Jr.  
d.d.boyd@nasa.gov

Joelle Bailly  
joelle.zibi@onera.fr

Yves Delrieux  
yves.delrieux@onera.fr

Italo Cafarelli  
italo.cafarelli@onera.fr

Yasutada Tanabe  
tan@chofu.jaxa.jp

Hideaki Sugawara  
sugawara.hideaki@jaxa.jp

Sung N. Jung  
snjung@konkuk.ac.kr

Seong H. Hong  
shsky0721@konkuk.ac.kr

Do-Hyung Kim  
dhkim@kari.re.kr

Hee J. Kang  
hkang@kari.re.kr

George Barakos  
george.barakos@glasgow.ac.uk

Rinaldo Steininger  
2238057S@student.gla.ac.uk

<sup>1</sup> DLR, Brunswick, Germany

<sup>2</sup> US Army DEVCOM AvMC, NASA Ames Research Center, Mountain View, CA, USA

<sup>3</sup> NASA Langley Research Center, Hampton, VA, USA

<sup>4</sup> ONERA, Paris, France

<sup>5</sup> JAXA, Tokyo, Japan

<sup>6</sup> Konkuk University, Seoul, Korea

<sup>7</sup> KARI, Daejeon, Korea

<sup>8</sup> University of Glasgow, Glasgow, UK

$C_T$	Thrust coefficient = $T/(\rho A[\Omega R]^2)$
$EI_{x,z}$	Rotor blade flap, lead-lag stiffness, $\text{Nm}^2$
$F_{x,y,z}$	Rotor hub forces in streamwise, starboard, and vertical direction, N
GJ	Rotor blade torsion stiffness, $\text{Nm}^2$
$L/D_e$	Rotor equivalent lift/drag ratio
$m_b$	Rotor blade mass, kg
$m, n$	Integer multiplier
$M$	Mach number
$M_{\text{off},n}$	Active twist moment offset and np amplitude
$M_{x,y}$	Rotor hub rolling and pitching moment, Nm
$N_b$	Number of rotor blades
$p$	Per rotor revolution
$P$	Rotor power, kW
$r$	Rotor blade radial coordinate, m
$R$	Rotor radius, m
$T$	Rotor thrust, N
$V_\infty$	Wind speed, m/s
$W_0$	Virtual helicopter weight, N
$x, y, z$	Rotor blade coordinate system: chordwise, radial, vertical; rotor hub coordinate system: downstream, starboard, vertical, m
$\alpha_S$	Rotor shaft angle of attack, $^\circ$
$\gamma$	Virtual flight path angle, $^\circ$
$\Theta_{75}$	Collective blade pitch control angle, $^\circ$
$\Theta_{S,C}$	Longitudinal and lateral cyclic pitch control angle, $^\circ$
$\mu$	Advance ratio, = $V_\infty/(\Omega R)$
$\rho$	Air density, $\text{kg/m}^3$
$\sigma$	Rotor solidity, = $N_b c/(\pi R)$
$\phi_n$	Phase angle of np active twist control, $^\circ$
$\psi$	Rotor blade azimuth angle, $^\circ$
$\Omega$	Rotor rotational speed, rad/s

### Abbreviations

ATR	Active twist rotor
BVI	Blade–vortex interaction
BVISPL	BVI sound pressure level, dB
CFD	Computational fluid dynamics
CFRP	Carbon fiber reinforced polymer
CSD	Computational structural dynamics
DIC	Digital image correlation
FM	Figure of merit in hover
GFRP	Glass fiber reinforced polymer
HHC	Higher harmonic control
HOST	Helicopter overall simulation tool (of Airbus Helicopters)
HSI	High-speed impulsive noise
IBC	Individual blade control
LED	Light-emitting diode
MFC	Macrofiber composite
OASPL	Overall sound pressure level, dB
RPM	Rounds per minute, 1/min

STAR	Smart twisting active rotor
VI	Vibration index

## 1 Introduction

After World War II, helicopters were increasingly introduced into many specialized operations that could not be served by fixed-wing aircraft. Today, these operations include service for offshore, commercial, civil, and military applications, search and rescue, and many others. Helicopters combine the generation of lift and propulsive force in one main element: the main rotor with several blades revolving around the hub. The aerodynamic environment of rotating blades in forward flight inherently generates a large bandwidth of unsteady aerodynamic forces and moments acting on them. Their dynamic response depends on their flexibility, dynamic characteristics, and on the type of attachment to the hub. It includes motions in all their degrees of freedom: rigid and elastic blade flap, lag, and torsional motion. Centrifugal forces acting on the rotating blades in motion further introduce steady and dynamic loads and inertia couplings between the various blade degrees of freedom.

In steady flight, all these unsteady blade aerodynamic and inertial forces and moments are repetitive each revolution and thus can be represented as integer multiples,  $n$ , (so-called harmonics) of the rotor fundamental rotational frequency,  $\Omega$ . At the rotor hub, the forces and moments introduced by all the blades are additive and are transmitted via the rotor shaft to the fuselage of the helicopter. This superposition of a wide range of harmonic loads at the hub and the transformation into the nonrotating helicopter frame results in vibratory forces and moments that consist of integer multiples,  $m$ , of the fundamental frequency,  $\Omega$ , times the number of blades,  $N_b$ .

Depending on the operational condition, the blade tip vortices trailed into the rotor wake form a spiral that can be close to all blades of the rotor. This happens especially during landing approach in descending flight, when the rotor inflow due to flight speed is oriented upward and is of the same order as the thrust-induced inflow. Blade–vortex interactions (BVI) develop in a large variety of geometries with respect to the individual's vortex axis orientation relative to the interacting blade leading-edge orientation in space. The phenomenon when the blade leading edge and the vortex axis are parallel with very little vertical distance between them is of special interest. This generates fast and strong modifications of the blade surface pressure distributions. These rapid modifications to surface pressure happen when vortices—with their high swirl velocities and small vortex core dimensions (significantly smaller than the blade chord length)—pass the blade quickly. Consequently, strong impulsive noise is radiated, especially downward.

Compared to fixed-wing aircraft, the helicopter vibration levels are much higher. They affect the crew and passengers adversely and reduce the lifetime of mechanical components. The noise radiation especially during landing approach near the ground is a concern for the outside environment and is also a certification issue of helicopters. Because of the above, both vibration and noise reduction have been a major issue since helicopters entered service. Because the rotor vibratory forces and moments are functions of the rotor harmonics and the number of blades, only a few rotor blade harmonics need to be controlled to reduce or eliminate vibration. Active rotor control has thus been under investigation since the 1950s, mostly by means of higher harmonic control (HHC) systems [1]. These are comprised of actuators underneath the swashplate and introduce the harmonics  $n = N_b - 1, N_b, N_b + 1$  to the rotor blade by proper phasing of the actuator motion. These actuator controls are superimposed on the pilot's controls, which also move the swashplate.

The advantage of these HHC systems is that all components are in the nonrotating frame of the fuselage and, with respect to certification and safety of operation, can easily be made redundant. A disadvantage to the HHC systems is that many masses (e.g., pushrods underneath the swashplate, the swashplate itself, the pitch link push rods, all the blade attachments, and all the inner parts of the blades) need to be moved with high frequency. Moving masses in this manner requires a large amount of power and makes the system heavy. Another disadvantage is the limited number of harmonics that can be transmitted to the rotor blades by the kinematics of the swashplate. This type of HHC system is only effective for rotors with more than three blades, which is currently most helicopters with a gross weight of more than two tons.

Numerical investigations have shown that a blade control of twice per revolution ( $2p$ , or  $n = 2$ ) might be beneficial for rotor power reduction in fast-forward flight, and it was beneficial for reducing BVI noise in low-speed descent flight. To overcome the disadvantages of HHC systems, individual blade control (IBC) systems with actuators at or in every individual rotor blade were investigated soon after the HHC systems were examined [2]. These IBC systems are comprised of actuators above the swashplate, for example, replacing the pitch link push rods. Still, the blade root attachments and inner part of the blade must be moved with high frequency. However, IBC systems can control any frequency on all blades and can also have different controls between the blades (if needed, e.g., for in-flight blade tracking).

On-blade controls like trailing edge flaps are also considered IBC systems, with the further advantage that trailing edge flaps move only a very small device at the location where it is most effective, thus requiring significantly less power than a blade root control system. The disadvantage of

IBC systems is that they all need power (often hydraulic) and signal transmission between the nonrotating and the rotating frame. Such a system is difficult to make redundant for safety and is therefore a major certification issue. In addition, these systems have mechanical components moving under large centrifugal forces that often were found biasing the controls significantly.

Recently, an IBC system capable of controlling every blade individually with all actuators still underneath the rotor was invented by DLR. This system comprised a multiple-swashplate control such that, for up to three blades of a rotor, one swashplate needs to be installed. For example, rotors with one to three blades require one swashplate; rotors with four to six blades require two independent swashplates; and rotors with seven to nine blades require three independent swashplates. It was tested successfully with a four-bladed rotor [3] and a five-bladed rotor [4] in the German-Dutch wind tunnel (DNW) large low-speed facility (LLF). The advantages of that system are that the entire system is in the nonrotating frame, all IBC capabilities are achieved, and redundancy can be obtained. The disadvantages are that the weight penalty and mechanical complexity grow with several swashplates instead of one, and three actuators per swashplate are required.

To avoid many of the disadvantages of IBC systems, active twist control of helicopter rotor blades was initiated around 1990 using smart materials as actuators. Several survey papers showing different applications of these materials were published in recent years [5, 6]. One of the concepts, active twist of rotor blades, appears most promising because it twists the blade by introducing torsional moments along its span. The active twist is introduced by macrofiber composite (MFC) actuators embedded in the skin of rotor blades that are based on piezoceramic materials. These MFC actuators can expand or contract, even at high frequencies, when a voltage is applied across them. Distributed and oriented appropriately on the upper and lower surface of the blade, they can act as a sort of artificial muscle, which can elastically twist the entire blade by introducing torsional moments all along the actuated region.

Such a system was first demonstrated by the National Aeronautics and Space Administration (NASA)/Army/MIT Active Twist Rotor (ATR) project [7–14]. The advantages of active twist systems are that no mechanical parts are present, only the aerodynamic active parts of the rotor blade are actuated, and the airfoils remain unchanged. The disadvantages are that electric energy must be transmitted into the rotating frame, no redundancy of actuators is easily possible, and the MFC actuator material increases the blade weight. The ATR was successfully tested in the heavy gas, variable density test medium of the NASA Langley Transonic Dynamics Tunnel by means of an aeroelastically scaled, four-bladed model rotor of 1.4 m radius, 0.107 m chord,  $-10^\circ$  pre-twist, a tip

Mach number of 0.6, and a relatively high natural frequency of torsion above  $7p$ . Hovering tests were performed in 1999 in the closed test section [9] evaluating the active twist performance with respect to statically and dynamically twisting the blade, and tests with wind followed in 2000 mainly for investigation of vibration reduction by means of active twist control [10, 11].

Advance ratios from 0.14 (with a shaft angle sweep) to 0.367 (level flight) were executed without actuation (baseline) and with an active twist control using  $3p$ ,  $4p$ , and  $5p$ , respectively. Fixed-frame vibratory loads could be reduced by 60–95%, and  $3p$  control was found most effective, confirming the results of many HHC and IBC tests performed before [1, 2]. The actuators were spanning from 30 to 98% radius and were able to introduce up to  $1.4^\circ$  twist amplitude with 1000 V amplitude input at each of the control frequencies. Because of the very high blade natural frequency in torsion, the control frequencies used could not make use of torsional amplification that might have been possible if the blade natural frequency had been closer to the active twist control frequencies.

In the early 1990s, DLR started active twist rotor investigations, initially focusing on extension–torsion coupling based on a discrete actuator in the blade tip region [15]. Later examinations used the skin-embedded MFC actuator concept like the ATR. After several prototypes were built and whirl tower tested, the smart twisting active rotor (STAR) project originated in 2007 [16, 17]. The goals were to build and test a large highly instrumented Mach-scaled model rotor with an active twist capability for investigation of vibration, noise, and power reduction and to compare results to HHC and IBC tests performed previously. After individual bench tests with each blade [18], the effort progressed to a test with all four blades on the DLR rotor test rig in 2013 [19]. Predictions were performed for the test matrix, clarifying the possible benefits of active twist [20–22].

However, the test with all four blades on the rotor test rig revealed strains that were too large for the actuators, resulting in many local cracks in the actuator's ceramics and in the overloading of the high-voltage amplifiers. These issues finally led to the cancellation of the subsequently planned DNW-LLF test. They were caused by too large offset of the mass axis from the tension axis, leading to a forward bending due to centrifugal forces. After the redesign of the blade by stiffening the trailing edge with CFRP strips and replacing the main spar GFRP with CFRP, this issue was solved and the overall strains were reduced to a level that the actuators could carry without the previous types of actuator failures. This redesign was demonstrated with a prototype blade using a long-term whirl tower test under actuation [23–25].

A fully instrumented STAR set of redesigned rotor blades was built again and the individual blade whirl tower tests took place in 2022, followed by the pretest of the full rotor

on the rotor test rig in 2023. A new DNW test is currently planned for 2024 and prediction activities were again performed by all with the new blade design.

From 2005 until the present, the STAR activities were performed within an international team comprising DLR, NASA, US Army, ONERA, Konkuk University, Korea Aerospace Research Institute (KARI), Japan Aerospace Exploration Agency (JAXA), DNW, and recently the University of Glasgow.

The innovations of the STAR rotor design versus the ATR rotor are a significantly larger Mach scale model rotor with a much lower natural frequency of torsion than the ATR rotor. The twist efficiency was doubled, i.e., for the same voltage input about twice the amount of twist is achieved. The rotor blades are heavily instrumented with strain gauges and absolute pressure sensors. Its response in torsion is used to magnify active twist inputs at  $3p$  and  $4p$  control frequencies, thus requiring less voltage for control inputs to achieve even higher blade tip twist amplitudes than the ATR rotor blades. Differences between the ATR and STAR tests are as follows: In addition to vibration reduction, investigations have a strong focus on BVI and HSI noise reduction, high-speed power reduction, high-load stall reduction, and high advance ratio conditions with slowed rotor RPM.

## 2 Star rotor blade

The blade geometry and airfoil of the STAR rotor are like the Bo105, but they are arranged in an articulated hub and rotate clockwise when looking at the rotor from above. The load-bearing structure of the blades consists of a carbon fiber reinforced polymer (CFRP) main spar fitted with balance weights in the nose area and CFRP straps near the trailing edge. To generate the active twist, 30 actuators have been integrated into the two-layer glass fiber reinforced polymer (GFRP) skin of each rotor blade.

Numerous strain gauges measure the strains in the flap and lead-lag bending and torsion directions. To measure the aerodynamic pressure distribution around the airfoil, a total of more than 200 pressure sensors are installed in the five STAR blades. Figure 1 shows the sensor locations and detailed information regarding the structure of the blades and the complex manufacturing process are described in Kalow et al. [24].

The rotor consists of  $N_b = 4$  blades with a radius  $R = 2$  m, a chord  $c = 0.121$  m, a rotor solidity  $\sigma = 0.077$ , and the blade mass  $m_b = 3.44$  kg (without blade clamp, including an amplifier box attached to the root). Due to the actuators and instrumentation, the STAR model rotor blade is significantly heavier than the Bo105 model rotor blade.

The final blades were investigated for blade stiffness and location of the elastic axis in a specialized test stand shown

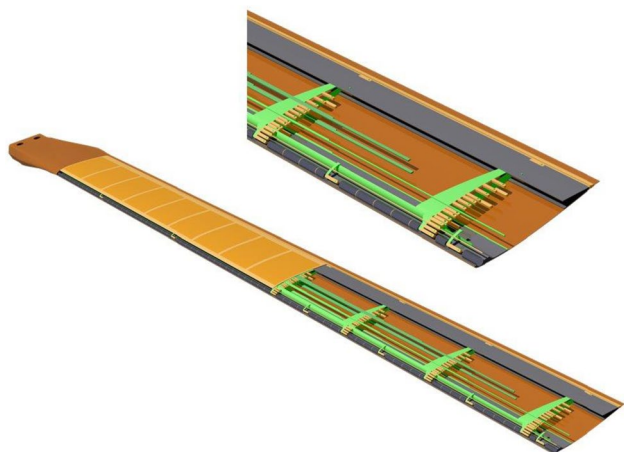


Fig. 1 Detailed rotor blade design with pressure sensor locations



Fig. 2 Laboratory testing of blade stiffness [source: DLR]

in Fig. 2. This test stand enables the rotor blade in vertical alignment and clamped at the root to be loaded with forces in the bending direction at different chordwise positions. A dedicated displacement measurement using a digital image correlation (DIC) system allows correlation between forces and displacements, which allows for the determination of the blade stiffness.

Figure 3 shows the stiffness in torsion (GJ) and flap bending ( $EI_x$ ) of the five rotor blades in comparison to the average of all experimentally determined blade properties. Lead-lag bending stiffness ( $EI_z$ ) was not measured in the lab.

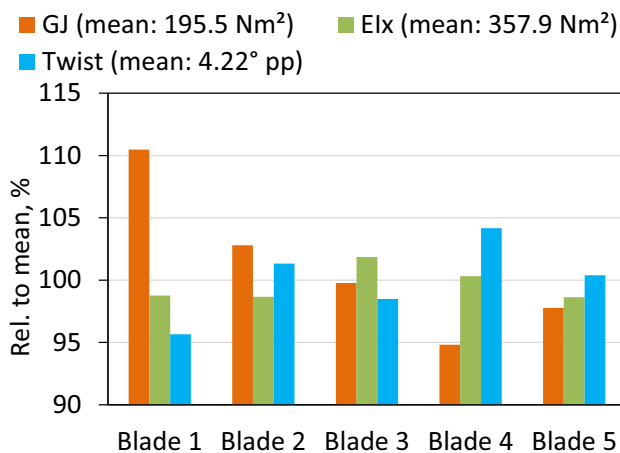


Fig. 3 Comparison of experimental STAR blade properties (deviation from averages given above)

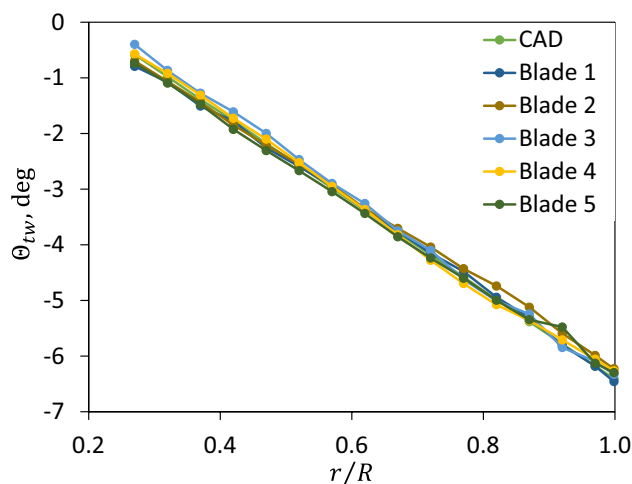


Fig. 4 Measured built-in twist distribution

These mainly show the similarity of all the blades within 5% of the average, which is an essential element for the operation in the wind tunnel. Another important point is that the performance of the actuators is very similar in all blades and is already sufficient to achieve a twist of at least  $\pm 2^\circ$  that is required for all operating conditions and for all test goals of the test matrix.

Another important parameter for the blade-to-blade similarity is the built-in twist. To check this, a 3D scan of each blade was carried out. The analysis in Fig. 4 shows that the desired linear twist of  $-8^\circ$  over the blade span was achieved for all blades.

Following the laboratory tests, the individual blades were installed in the DLR whirl tower for integrity testing and actuation testing under centrifugal loads. Figure 5 shows this whirl tower with an installed rotor blade. For individual blade testing, a counterweight was used for balancing and



Fig. 5 STAR blade in the whirl tower [source: DLR]

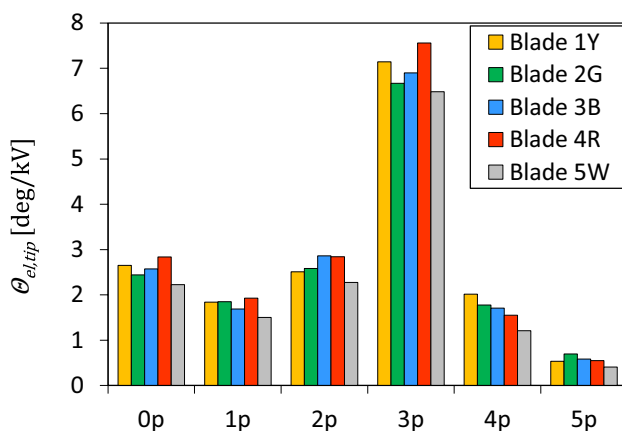


Fig. 6 Active twist capability of the STAR blade in the whirl tower at various actuation frequencies

the blade-integrated strain gauges were monitored. However, the most important is the blade tip pitch measurement, which was determined by images of the blade tip using an external camera.

To reference the blade tip more clearly, two LEDs are installed in the tip plane at the leading and trailing edges, respectively. These optical measurements are examined in a real-time LabVIEW analysis. Measurements are conducted for quasistatic excitation (0.15 Hz) and higher harmonics of  $1p$ ,  $2p$ ,  $3p$ ,  $4p$ , and  $5p$  of the nominal rotor speed. The results of this test are shown in Fig. 6, demonstrating the active twist capability under full centrifugal

loads. Near the natural frequency of torsion (which is different in the whirl tower than on the rotor test rig), a significantly reduced excitation magnitude of only 300 V was needed to achieve the goal of  $2^\circ$  blade tip twist amplitude, and the data of  $3p$  in the figure are extrapolated to an excitation of 800 V.

These measurements serve as an additional check of the blade motion and system test for the actuators and the sensors installed. These sensors also serve as a risk reduction measure for the first rotor test with this setup and for the wind tunnel. The rotating hardware and the control software were also tested during these measurements. Components of the final control software running in LabVIEW were used.

### 3 Test matrix and codes applied

#### 3.1 Test matrix

The test matrix anticipated so far for the STAR rotor will be executed in the  $6\text{ m} \times 8\text{ m}$  open jet configuration of the DNW-LLF. It will cover the following operational conditions: reference baseline, BL, without actuation for measurement of the passive rotor and with an active twist for evaluation of its impact on the respective parameter(s) of interest.

The operational conditions are limited by the available motor power limit, maximum balance and component loads, and the wind tunnel speed range. The lower speed limit is defined by slipstream deflections caused by the rotor thrust and depends on the cross-sectional size of the model and on the presence or absence of the wind tunnel walls.

For the  $6\text{ m} \times 8\text{ m}$  open jet configuration chosen for this test and using a nominal rotor thrust of 3600 N, the wind tunnel lower speed limit is estimated to be about  $V_\infty = 20\text{ m/s}$ . The maximum attainable wind speed is about  $V_\infty = 78\text{ m/s}$ . Within the test matrix, the selected wind speed will be 0 m/s (hover) and 22 m/s to 76 m/s, leading to blade tip speed ratios of  $V_\infty/(\Omega R) = 0.0, 0.1, \text{ and } 0.35$ , respectively, at 100% RPM and up to 0.7 at 50% RPM. The test matrix is comprised of the following conditions:

- Hover at  $V_\infty = 0\text{ m/s}$  with a thrust sweep for evaluation of the figure of merit (FM). The steady active twist with a  $0p$  harmonic applied for FM improvement.
- Level flight with  $V_\infty = 22\text{ to }76\text{ m/s}$  wind speed and up to three different rotor loadings for code validation, passive rotor only.
- Flight path variation ( $\gamma$ -sweep) at 33 m/s with identification of the maximum BVI noise radiation condition. Application of  $2p$ ,  $3p$ ,  $4p$ , and  $5p$  active twist harmonics for evaluation of BVI noise reduction and vibration reduction.

- High load at 33 m/s investigating vortex-induced stall of the rotor at 50% nominal RPM,  $V_\infty/(\Omega R) = 0.3$ . Active twist with a  $2p$  harmonic for stall alleviation.
- High speed at 76 m/s with a focus on power, vibration, and high-speed impulsive (HSI) noise radiation. Active twist with  $0p$ ,  $1p$ , and  $2p$  harmonics for power, vibration, and HSI noise reduction.
- High advance ratio of  $\mu = 0.7$  at 50% RPM with a variation of the shaft angle ( $\alpha_s$ -sweep). Application of  $0p$  and  $2p$  active twist harmonics at  $0^\circ$  and  $180^\circ$  phase for evaluation of its impact on power and vibrations. At  $\alpha_s = 0^\circ$ , an active twist application with a  $2p$  harmonic and a phase sweep.

For level flight and the flight path variation (moderate climb to steep descent), the rotor trim is performed for rotor lift  $L$  (= scaled weight  $W_0$ ) and propulsive force  $F_x$  (in wind axis, positive downstream) to overcome a virtual fuselage drag. Alternatively, a trim to their equivalent in the rotor shaft axis system can be performed, which is inclined such that the resultant of lift and propulsive force are in line with the shaft axis. Thus, the shaft axis force  $F_z = T$  and  $F_x = 0$  N ( $F_x$  positive downstream). In either case, the hub rolling moment in the shaft axis system is trimmed to zero:  $M_x = 0$  Nm.

The high-load condition with vortex-induced stall represents a high-g maneuver in cruise flight with a shaft angle fixed to  $\alpha_s = 0^\circ$  in the wind tunnel. Due to the loads exceeding the balance limits at full RPM, the trim is performed at half RPM with zero hub moments. The high advance ratio condition represents a slowed rotor with half RPM at full wind speed of 76 m/s. A tip speed ratio of almost  $\mu = 0.7$  is obtained. Here, the collective control angle is fixed to  $\Theta_{75} = 4^\circ$ , a shaft angle sweep performed from  $\alpha_s = -4^\circ$  to  $+4^\circ$ , and the rotor trimmed to zero hub rolling and pitching moments in the shaft axis system by means of the cyclic control angles.

Whenever active twist is employed, a retrim of the rotor to the desired operational condition is performed. In case of the high advance ratio (50% RPM) conditions with an active twist, the thrust is also retrimmed to the value obtained by the passive rotor using the collective control angle.

Operational limits were computed using the DLR S4 comprehensive rotor code (described in the following section) covering all the passive rotor and active twist conditions. Figure 7 exemplarily shows the rotor power expected in the various conditions.

Wind speeds between 0 and 20 m/s cannot be run with nominal thrust due to excessive deflection of the airflow and associated wall corrections, and 76 m/s is the maximum achievable wind speed in that test section with the rotor model in it. The rotor drive system has a power limit

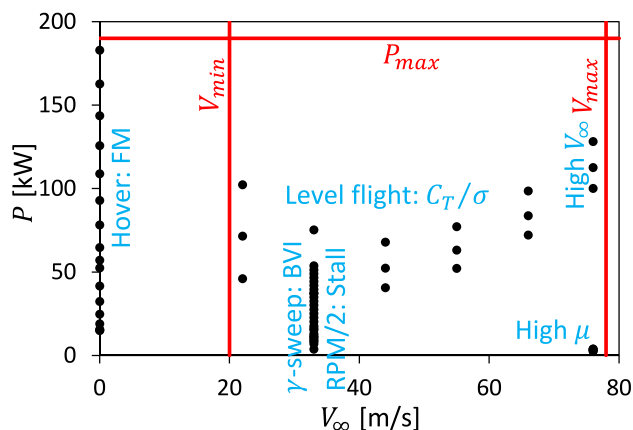


Fig. 7 Power required for the test matrix conditions

of  $P_{max} = 190$  kW, limiting the hover condition (used to measure a figure of merit curve). All test conditions are in the available range of the wind tunnel and rotor test rig capabilities, and hover is limited by the available motor power.

Hover testing at DNW is possible due to the absence of wind tunnel walls around the rotor, and its height of roughly 10 m above ground eliminates the ground effect. However, the test hall—despite its huge dimensions—represents a volume closed on all sides such that some recirculation will develop, in proportion to the rotor thrust, which effectively generates an unavoidable slow vertical climbing condition. Pretest predictions ignore this recirculation effect until measured data are available and focus on the hover Figure of merit (FM). FM is defined by the ratio of ideal power (based on momentum theory) that is related to the total power consumed  $P_{tot}$ , Eq. (1), wherein  $T$ ,  $\rho$ ,  $A$ , and  $R$  are the rotor thrust, air density, rotor disk area, and the rotor radius, respectively.

$$FM = \frac{\sqrt{T^3/(2\rho A)}}{P_{tot}}; \quad A = \pi R^2 \quad (1)$$

Rotor vibration is measured by the rotor balance. The hub loads in the nonrotating frame (horizontal force  $F_x$ , lateral force  $F_y$ , vertical force  $F_z$ , rolling moment  $M_x$ , and pitching moment  $M_y$ ) are analyzed for their  $4p$  and  $8p$  components. Following Crews [26], a vibration intrusion index, VI, is used as a nondimensional measure of vibration.

For computing VI, the  $ip$  ( $i = 4, 8$ ) hub forces  $F_{x/y/z,i}$  are weighted by a factor of 0.5, 0.67, and 1, respectively, and referenced to a virtual model-scale weight of  $W_0 = 3600$  N, while the  $ip$  hub moments  $M_{x/y,i}$  are referenced to  $RW_0$ ; see Eq. (2).

$$VI = \sum_{i=4,8} \frac{\sqrt{(0.5F_{x,i})^2 + (0.67F_{y,i})^2 + (F_{z,i})^2}}{W_0} + \sum_{i=4,8} \frac{\sqrt{(M_{x,i})^2 + (M_{y,i})^2}}{RW_0} \quad (2)$$

### 3.2 Rotor codes employed

The computations under the various conditions were performed by a variety of codes of different fidelity levels, ranging from rotorcraft comprehensive analysis codes to loosely coupled CFD/CSD approaches. These are based on the delta airload method as demonstrated in Refs. [37] and [38], the latter solving for the phase lag of the advancing side negative lift peak in fast-forward flight.

#### 3.2.1 DLR-CA

The DLR comprehensive analysis tool, S4, is a high-resolution, fourth-generation comprehensive rotor simulation code [27, 28]. The finite element-based structural dynamics modeling in S4 is based on Houbolt and Brooks equations [29]. The beam element has ten degrees of freedom. A semiempirical formulation of the airfoil coefficients based on the Leiss method [30] is used for unsteady blade motion, but further modification is made for the BVI problem. The fuselage interference flow effect is included at the blade sections using a semiempirically derived formulation from the potential theory [28].

The Mangler/Squire global wake model [31] is used for performance and vibration estimates, but an extended version of the Beddoes' prescribed wake geometry formulation [32] with multiple trailers is used for noise predictions, accounting for wake deflections due to harmonic rotor loading. Trim is performed with an azimuth increment of 1°, and the simulation uses the first six modes for a modal analysis. The noise radiation is computed using the acoustic code, APSIM [33], which is based on the Ffowcs Williams–Hawkings equations [34] and predicts the loading and thickness noise.

#### 3.2.2 DLR-CFD

The DLR-CFD approach is based on the coupling of the DLR legacy flow solver FLOWer [35] with the comprehensive code, HOST [36] (Airbus Helicopters), used using the delta airload approach [37, 38]. On the structural side, the first eight eigenmodes are included. The inviscid fluxes are resolved using a fourth-order upwind scheme (SLAU2 with FCMT) [39]. The SA-DDES-R [40, 41] turbulence model is applied for the computation of the eddy viscosity, and

the transition is empirically predicted [42]. A dual time-stepping approach with a time step equivalent to 1/4° of a revolution is used. The grid consists of 15 M grid points with a background grid spacing of  $\Delta x/c = 0.17$  in the vicinity of the rotor and 1 M grid points for each blade grid. For the determination of the acoustics, the code APSIM [33] by DLR is used. For the high-speed flight condition, the porous formulation is used, whereas for the other flight conditions the surface formulation is applied.

#### 3.2.3 ONERA-CA

Low-to-medium levels of fidelity are used at ONERA for aerodynamic and acoustic simulations. The low fidelity, finite element-based HOST [36] comprehensive code developed by Airbus Helicopters solves blade deformations. The aerodynamics model in HOST is based on a lifting line approach, for which the aerodynamic coefficients are directly interpolated using 2D semiempirical airfoil tables depending on the local sectional Mach number and the angle of attack. Theodorsen's unsteady aerodynamics are used, and the corrections for yaw flow and stall are available. Different inflow models are used, depending on flight condition.

For the hover configuration, the finite state unsteady wake model (FiSuW) is used that expresses the induced velocity by means of Legendre polynomials for the radial distribution and Fourier series for the azimuthal variation [43]. For the high advance ratio cruise configuration, the prescribed helical wake code, METAR [44], is used iteratively within the trim loop. For the high-load cruise configuration, the fully time marching unsteady wake model, MINT [45], developed at ONERA is used. The wake is discretized in panels of constant gradient of potential jump, which improves the accuracy and the stability of the method compared to the model of the wake by vortex lattices. For the descent configuration, the full-span, free-wake model MESIR [46], developed at ONERA, computes the velocities induced by all trailed and shed vortex lattices using the Biot–Savart law.

The roll-up of the vortices is modeled through the MENTHE [47] code, which determines the intensities and radial locations of the vortices at the emission azimuths. Blade pressure distribution is then calculated by the unsteady singularity method ARHIS [48]. Finally, the noise computation is performed using the acoustic code PARIS [49], based on the Ffowcs Williams–Hawkings equations [34]. It uses a time domain formulation and predicts the loading and thickness noise.

#### 3.2.4 US team, Konkuk University (KU), and KARI: CAMRAD II

The CAMRAD II comprehensive analysis code [50] was used by the US team [DEVCOM, Aviation & Missile Center

(AvMC), and NASA], KARI, and KU. The structural model is based on a finite beam element formulation with each element having nine degrees of freedom. The number of finite elements used in this study ranges from 8 to 18 elements.

The section aerodynamics is based on the lifting line theory with the C81 lookup table, and the ONERA EDLIN unsteady aerodynamic model is used. For the aerodynamics computation, 17 to 23 aerodynamic panels are used with a free-wake analysis. The trim solution is obtained at 15° azimuth. For noise calculations, the aerodynamic response is recomputed at a higher resolution of 5°, 1.5°, or 1° azimuth with the trim controls fixed (post trim). Noise calculation is performed using ANOPP2 Aeroacoustic Rotor Noise (AARON) tool [51] for the US partners and an in-house code based on the Ffowcs Williams–Hawkings equations [34] for KU and KARI.

### 3.2.5 KARI-CFD

The KARI-CFD tool is the 3D unsteady viscous flow solver based on unstructured meshes, UMAP3D [52], coupled with CAMRAD II. The flow solver utilized a vertex-centered finite volume scheme that is based on the Roe flux difference splitting with an implicit time integration. The eddy viscosity is estimated by the Spalart–Allmaras one-equation turbulence model. The overset mesh technique and the mesh deformation technique using the spring analogy method were adopted to handle the relative motion and deformation of the rotor blades. The blade deformation was calculated by CAMRAD II, and the rotor trim was iteratively solved in CFD and CSD codes until it matched the trim target.

### 3.2.6 JAXA

The JAXA computational fluid dynamics (CFD)/computational structural dynamics (CSD) coupled tool consists of three computational codes for rotary wing application—rMode, rFlow3D, and rNoise that were developed in-house at JAXA. The rMode code computes the natural frequencies and mode shapes of the blade flap, lag, and torsion modes that are based on Houbolt and Brooks equations [29].

The structured Navier–Stokes solver, rFlow3D, is based on a moving overset grid approach and adopts a modified simple low-dissipative advection upstream splitting method (mSLAU) to adjust numerical dissipation by limiting the drag at very low Mach number [53]. SST-2003 turbulence model with  $\gamma - \text{Re}_\theta$  transition model [54] is applied for present predictions. Blade deformation is solved using Ritz’s modal decomposition method and then is loosely coupled with the CFD solver.

Rotor trim controls are iteratively solved in the CSD routine until matching with the trim targets. After a periodically converged solution is obtained, the rNoise code computes

the noise generated by the rotor using Ffowcs Williams and Hawkings equations [34].

### 3.2.7 University of Glasgow (UofG)

The UofG in-house CFD/CSD framework Helicopter Multi-Block 3 (HMB3) is a finite volume solver on structured multiblock grids [55]. An overset grid method is used. HMB3 solves the unsteady Reynolds-averaged Navier–Stokes (URANS) equations in integral form using the arbitrary Lagrangian–Eulerian (ALE) formulation for time-dependent domains, including moving boundaries. To evaluate the convective fluxes, the Osher [56] approximate Riemann solver is used, while the viscous terms are discretized using a second-order central differencing spatial discretization.

The MUSCL approach developed by van Leer [57] is used to provide high-order accuracy in space with the alternative form of the van Albada limiter [58] in regions of large gradients. The implicit, dual time-stepping method of Jameson [59] is employed. The linearized system of equations is solved using the generalized conjugate gradient method with a BILU factorization as a preconditioner [60]. From one-equation to four-equation turbulence models are available in the HMB3 solver.

The 1994  $k - \omega$  SST model of Menter [61] is used in the predictions of the STAR rotor. The structural model solves for the linear scaling factors of the given number of precomputed eigenmodes as a function of time [62]. Active twist can be applied via prescribed mesh rotation or in MSC NASTRAN through a torsion moment in 1D beams or through a thermal analogy method in 3D-FEM. In steady simulations, beam deformations are directly computed from aerodynamic loads.

## 3.3 Active twist application

In the experiment, the active twist is performed by application of steady (offset) and periodic voltage. The offset is needed due to the asymmetric voltage range of the actuators and amounts to 400 V, resulting in  $M_{\text{off}} = 2.08$  Nm torsional moment along the actuated span of the blade. Including a safety margin, a dynamic range of 1000 V (5.2 Nm) relative to the offset could be used (= 100%), but only 50% (500 V; 2.6 Nm) and 80% (800 V, 4.16 Nm) will be used during dynamic actuation. In numerical simulations, the resulting torsional moments are applied by including a torsional moment couple near the inner and outer edges of the blade where the actuators end, for  $n = 0, 1, \dots, 5$ :

$$M(\psi) = M_{\text{off}} + M_n \cos(n\psi - \phi_n). \quad (3)$$

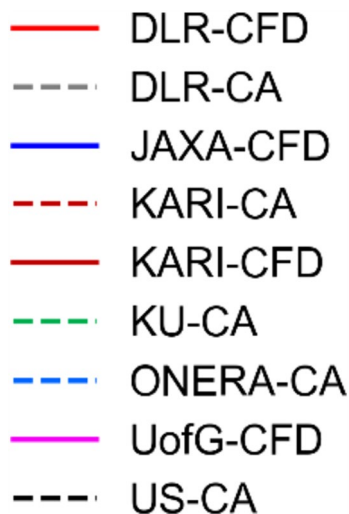


**Fig. 8** Universal line legend for the paper

Then, the voltage range for any individual np control input is composed of the + 400 V offset and the magnitude at np, for example, when using the 50% magnitude ranges from – 100 to +900 V, for the 80% magnitude from – 400 to +1200 V.

The power provision is quite heavy, and high-voltage amplifiers are mounted on top of the rotor hub. In this experimental setup as a technology demonstrator, this is considered acceptable, and an industrial maturation would reduce size and weight significantly, but that is out of the scope of STAR.

Since many partners are involved in this project and the plots tend to have many lines, it was decided to place the legend of these graphs here to make them visible in the remainder of the paper; see Fig. 8. Continuous lines represent CFD-based results, and dashed lines represent pure comprehensive code results.

#### 4 Hover: figure of merit

Hover performance together with the elastic deformations is predicted using high-fidelity methods (CFD) and comprehensive analyses. The rotor figure of merit (FM) predictions by the six partners are shown in Fig. 9. Acceptable agreements are obtained among these various prediction methods.

Elastic deformations with the change of blade loading are predicted with more scatter among the partners' results. The flap deformations predicted are almost agreeable among the partners as shown in Fig. 10. However, large differences are observed in the tip torsional deformation as shown in Fig. 11. It is noteworthy that even for this simple test condition, the satisfactory agreement cannot be found between the partners. This figure highlights the necessity of further

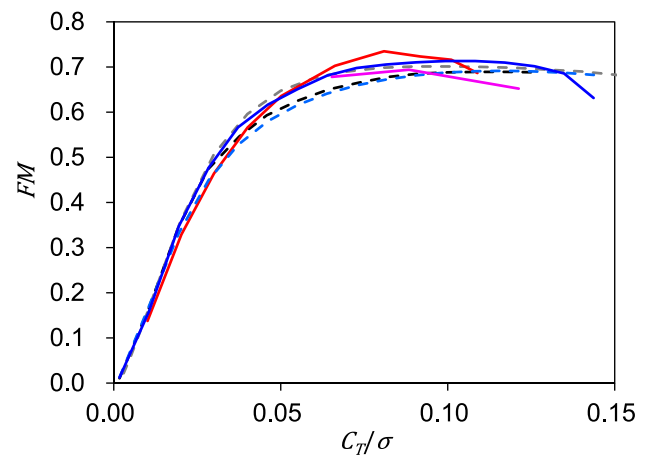


**Fig. 9** Figure of merit (FM) prediction

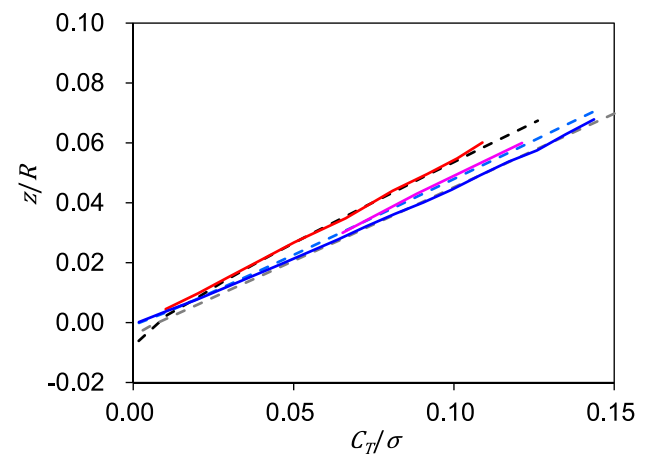


**Fig. 10** Flap deformation at the blade tip

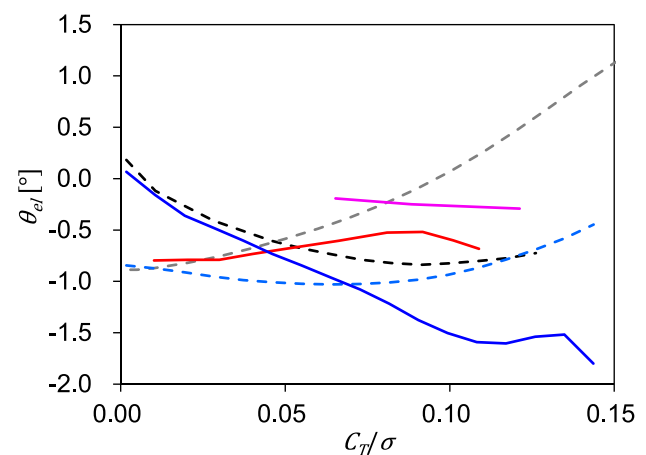


**Fig. 11** Torsion deformation at the blade tip

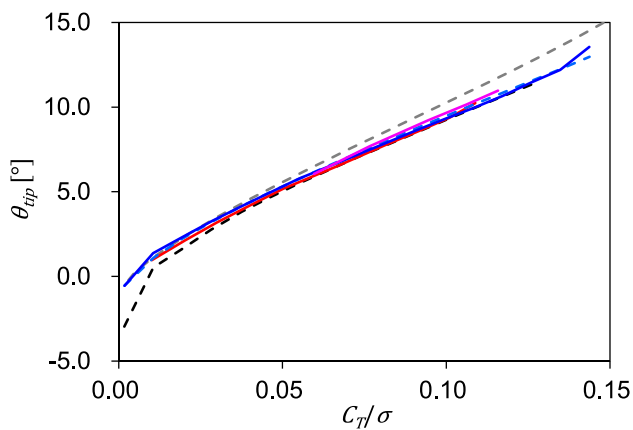


Fig. 12 Pitch angle at the blade tip

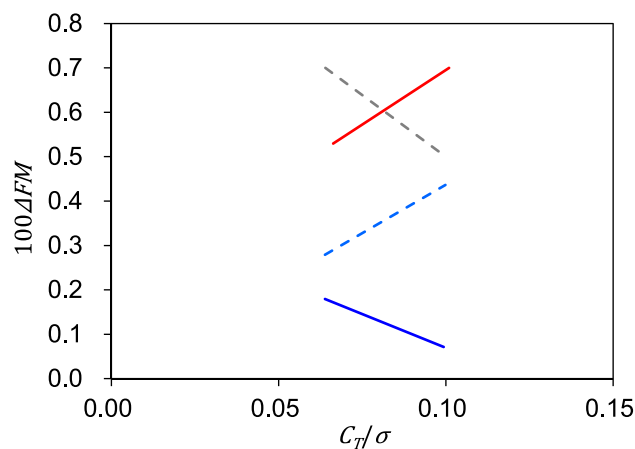


Fig. 14 FM improvement with static actuation

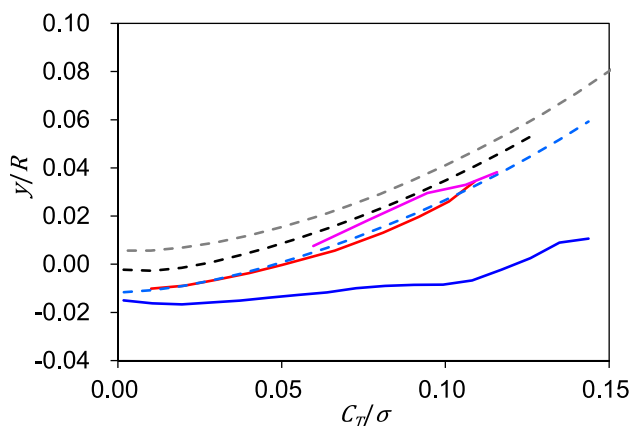


Fig. 13 Lag displacement at the blade tip

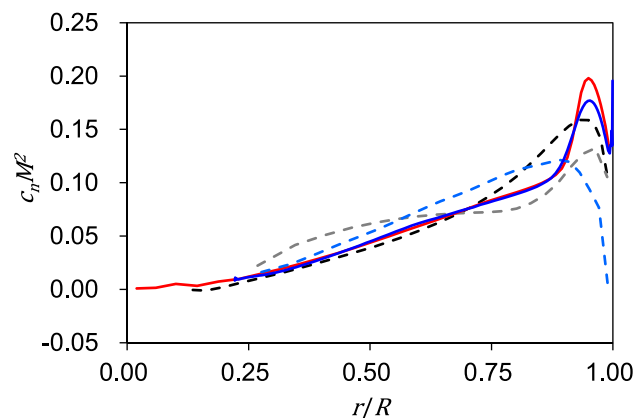


Fig. 15 Radial distribution of the sectional normal force for  $C_T/\sigma = 0.064$

improvements of the CSD codes and the need for validation with the measurements.

However, the blade pitch angles, which are the summations of the collective pitch angles and the elastic torsional deformations, as shown in Fig. 12, are in good agreement between the partners. The elastic twists predicted by the partners are within 10% of the built-in pre-twist angle of the blade, while the resultant blade pitch angle is strongly correlated with the thrust coefficient.

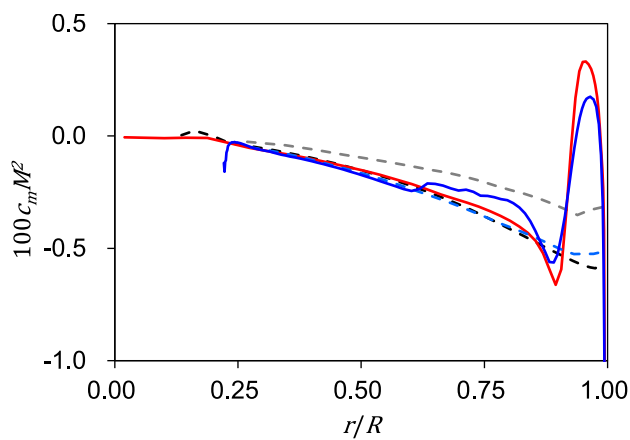
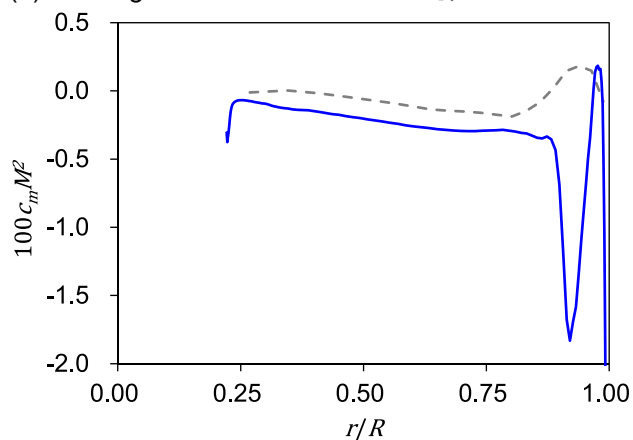
The lag deformations at the blade tip, as shown in Fig. 13, are more scattered, with most methods displaying a similar trend of increasing with thrust, but JAXA-CFD predicted a much lower increase. Validation with the experimental measurements of the blade deformations is expected after the test.

The effect of static active twisting of the blade at nominal blade loading  $C_T/\sigma = 0.064$  and 0.1 is examined by the partners. As shown in Fig. 14, only 0.07% to 0.7% of improvements of the FM are predicted when 80% of the full negative

blade twist amplitude with 400 V offset (actual static actuation of  $-400$  V, negative voltage causes nose-down twist) is applied.

To further clarify the differences in aerodynamic modeling utilized by the partners, comparisons of the radial distributions of the sectional normal force coefficient  $C_n M^2$  for  $C_T/\sigma = 0.064$  are shown in Fig. 15. The distributions of  $C_n M^2$  near the blade tip region remarkably change depending on the fidelity of the utilized prediction tool. The CFD results by DLR and JAXA showed an abrupt variation corresponding to the formation of a tip vortex. The comprehensive tools utilizing tip loss modeling by DLR and ONERA show a simple decrease of aerodynamic loading toward the tip. The US team using a free-wake modeling shows an intermediate variation near the blade tip.

Variation of the sectional pitching moment around the blade tip region is more sensitive to flow separation. As shown in Fig. 16a, at the nominal target thrust condition of  $C_T/\sigma = 0.064$ , the pitching moment coefficient  $C_m M^2$

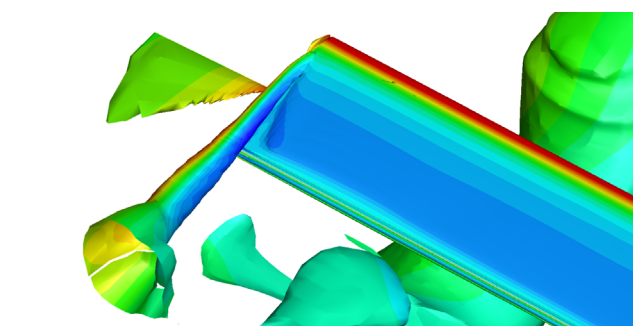
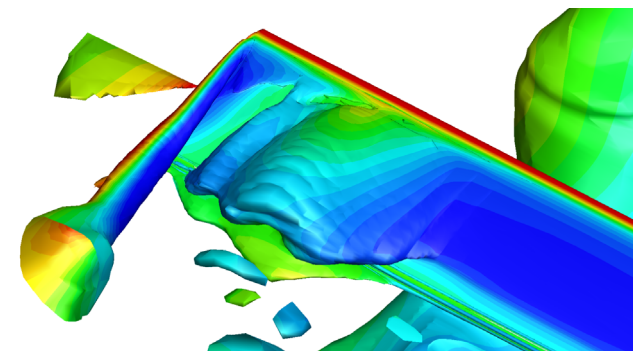
(a) Pitching moment coefficient for  $C_T/\sigma = 0.064$ .(b) Pitching moment coefficient for  $C_T/\sigma = 0.144$ .**Fig. 16** Sectional pitching moment distributions

shows a small decrease before increasing to a positive nose-up value near the blade tip as predicted by the CFD solvers. Such an abrupt change is not predicted by the comprehensive codes. When an obvious separation region forms at a large thrust condition of  $C_T/\sigma = 0.144$ , a sharp decrease of the pitching moment is observed, as shown in Fig. 16b.

The associated flow fields computed by CFD are represented by the isosurface of Q-criterion in Fig. 17. A local flow separation area is observed on the upper surface of the blade when  $C_T/\sigma = 0.144$ .

## 5 Descent: BVI noise and vibration

It is desirable to assess the effect of active twist on blade–vortex Interaction (BVI) noise at a flight condition where BVI noise is a maximum. BVI noise here is defined as the unweighted, overall sound pressure level (OASPL) of the 6th through the 40th blade passage frequency (BPF). The OASPL restricted to this frequency range is known as BVISPL. OASPL and BVISPL both have units of decibel

(a) Tip vortex for  $C_T/\sigma = 0.064$ .(b) Tip vortex for  $C_T/\sigma = 0.144$ .**Fig. 17** Isosurfaces of Q-criterion around blade tip region (JAXA results)

(dB). The first step is to determine the flight condition on approach (flight path angle) at which BVI noise is a maximum. The flight path angle  $\gamma$  was varied from a  $6^\circ$  climb ( $\alpha_S = -8.1^\circ$  forward shaft tilt) to a  $12^\circ$  descent ( $\alpha_S = 9.9^\circ$  aft shaft tilt).

Figure 18 shows a sample baseline (passive rotor, BL) computation for BVISPL on a horizontal plane, which is  $1.1R$  below the rotor hub. The maximum BVISPL value is seen on the left side of the figure, which is the advancing side of the rotor. The US, KARI, ONERA, and DLR teams computed plots such as those seen in Fig. 18 for the flight path angle variation described above. Each team extracted the maximum value of BVISPL from their predictions as a function of flight path angle. To compare the maximum BVISPL as a function of flight path angle from each partner, the largest of these maxima from each partner was subtracted from their respective results.

Figure 19 shows the change of noise level ( $\Delta$ BVISPL) relative to the maximum BVISPL as a function of flight path angle  $\gamma$  for each partner. Positive values of  $\gamma$  are for climbing flight. Negative values of  $\gamma$  are for descending flight. These show that the predicted flight path angle where the highest BVISPL occurs is between approximately  $-10^\circ$  and  $-7^\circ$  descent angle.

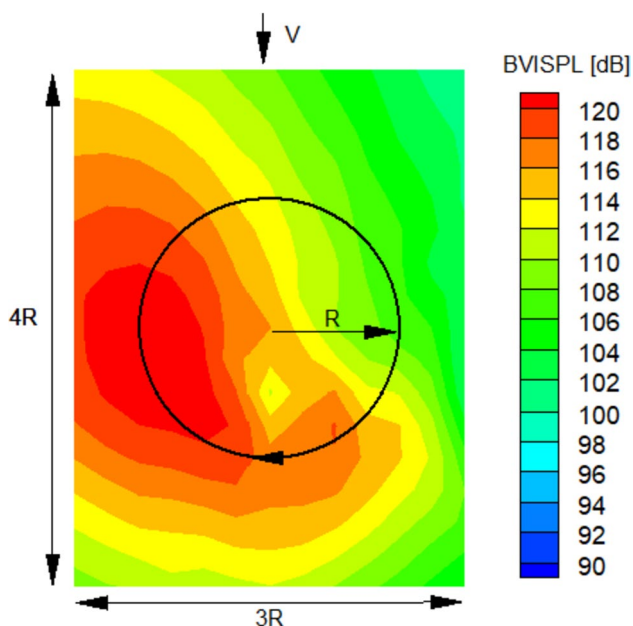


Fig. 18 Sample BVISPL [dB] calculation on a plane 1.1R below the rotor for the BL case. The black circle represents the extent of the rotor disk

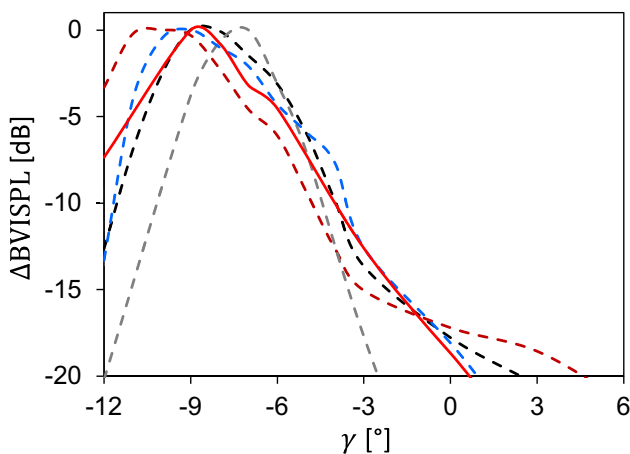


Fig. 19 Change of noise level relative to its maximum as a function of the flight path angle

In discussions with the partners, the decision was made to choose the 9° descending flight path angle ( $\alpha_s = 6.89^\circ$  aft shaft tilt) as the maximum BVISPL flight path angle. At this 9° descending flight path angle, active twist at frequencies equivalent to  $2p$ ,  $3p$ ,  $4p$ , and  $5p$  were applied, respectively. At each of the  $2p$ ,  $3p$ ,  $4p$ , and  $5p$  active twist frequencies, 50% and 80% of the maximum active twist amplitudes were applied at various azimuthal phases. The active twist is implemented as given in Eq. (3).

The US team performed  $2p$ ,  $3p$ ,  $4p$ , and  $5p$  active twist computations at both the 50% and 80% activation

amplitudes. The DLR-CA team performed computations for the same range of frequencies, but acoustic post-processing was only performed for the most promising conditions at a few selective phase angles for the  $2p$ ,  $3p$ , and  $4p$  at the 50% activation amplitude. The KARI team performed computations for  $2p$ ,  $3p$ , and  $4p$  at the 80% activation amplitude. The ONERA team performed computations with  $2p$  and  $3p$  at the 50% activation amplitude.

Figure 20 shows predictions using  $2p$  actuation at 50% and 80% amplitudes. The horizontal axis is the phase angle,  $\phi$ , as shown in Fig. 20, and the vertical axis is the change in BVISPL from the partners' respective maximum baseline BVISPL. There is a large variation of predicted results from the partners for the  $2p$  actuation. A trend is that many of the phase angles have predicted  $\Delta$ BVISPL to be near or less than zero. This tendency means that  $2p$  should slightly reduce the maximum BVISPL at many phase angles. For individual partner's results, a preferred phase angle can be determined where BVISPL is reduced. However, when examining partners' results collectively, there is not a clear indication of a preferred amplitude or phase angle when using  $2p$  active twist in this flight condition.

Figure 21 shows predictions using  $3p$  actuation at 50% and 80% amplitudes. The axis configuration is the same as that in Fig. 20. Here, too, there is a large variation of predicted results from the partners. Whereas the  $2p$  predictions tended to be below (or sometimes slightly above) zero, in the  $3p$  case, there appear just as many phases and amplitudes where the results are above and below the baseline maximum BVISPL.

As with the  $2p$  actuation, for individual partner's results for  $3p$  actuation, a preferred phase angle (or two) can be determined where BVISPL is reduced. However, when

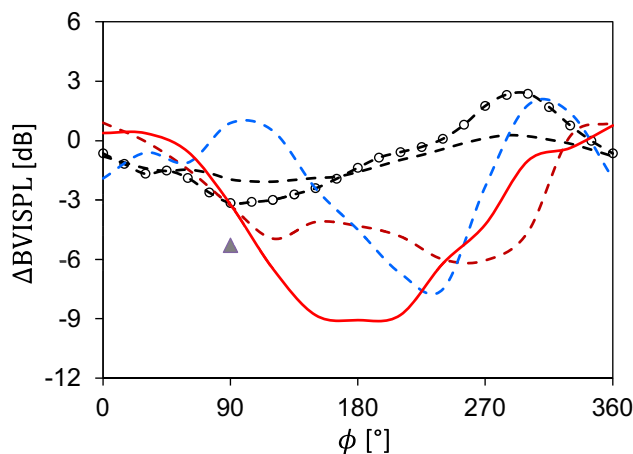


Fig. 20 Change of noise level relative to its maximum as a function of  $2p$  actuation with amplitudes of 50% and 80%. Dashed line with circles is the US 80% amplitude result. Triangle symbol is the result from DLR-CA

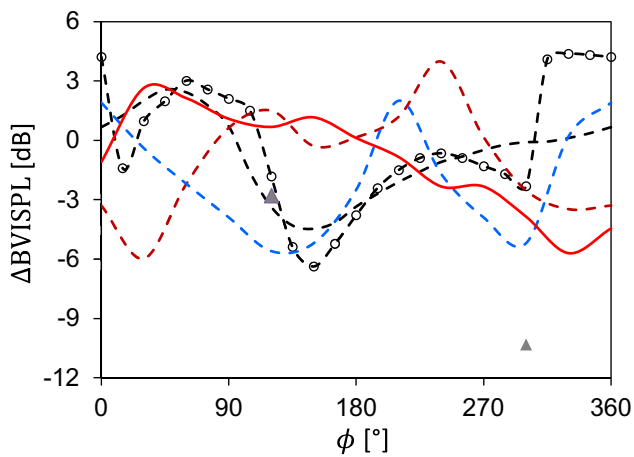


Fig. 21 Same as Fig. 20 for  $3p$  actuation

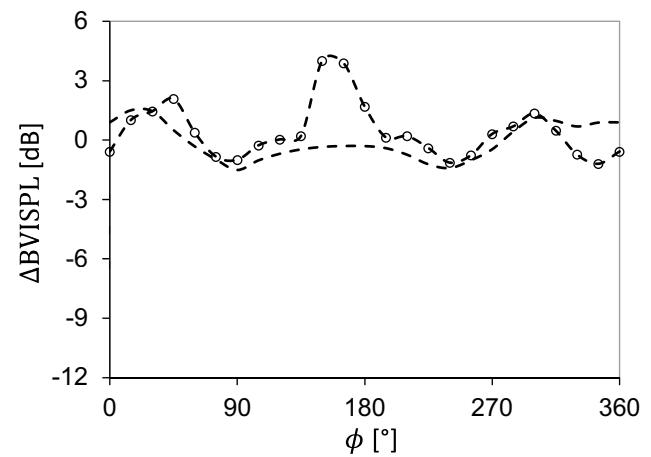


Fig. 23 Same as Fig. 22 for  $5p$  actuation

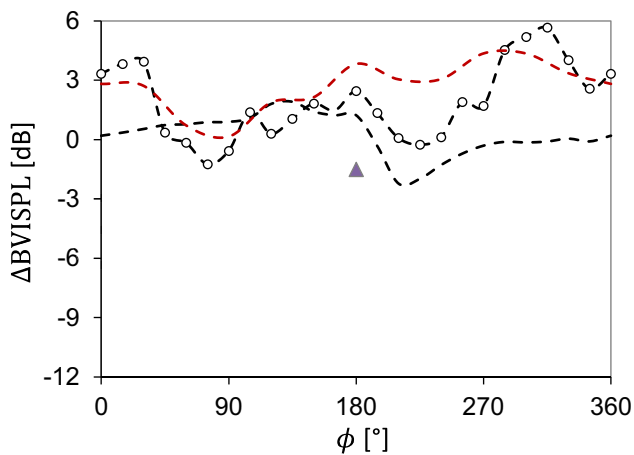


Fig. 22 Change of noise level relative to its maximum as a function of  $4p$  actuation with amplitudes of 50% and 80%. Dashed line with circles is the US 80% amplitude result. Triangle symbols are results from DLR-CA

examining partners' results collectively, there is not a clear indication of a preferred amplitude or phase angle when using  $3p$  active twist in this flight condition.

Figure 22 shows predictions using  $4p$  actuation at 50% and 80% amplitudes. In the  $4p$  case, there appear most phases and amplitudes where the results are above the baseline maximum BVISPL level. As such,  $4p$  active twist actuation does not appear to be a good candidate for this flight condition.

Figure 23 shows predictions using  $5p$  actuation at 50% and 80% amplitudes. There is no clear trend that indicates a preferred amplitude or phase of  $5p$  actuation. These predictions, as anticipated, indicate that usage of  $5p$  active twist will not be effective in the reduction of the maximum BVISPL for this flight condition.

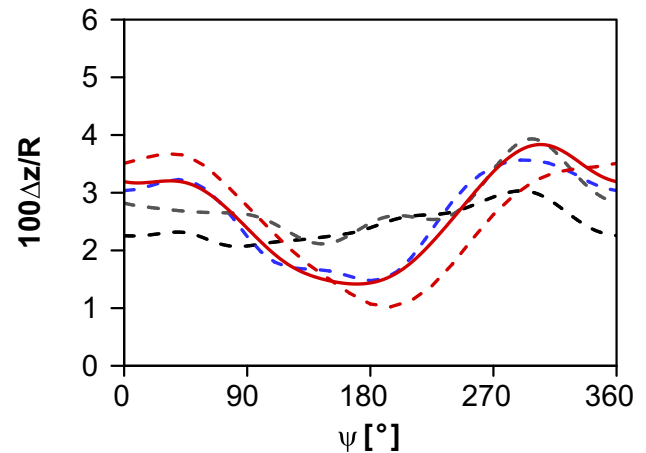


Fig. 24 Baseline tip flap motion as a function of azimuth angle

It is instructive to examine blade motion and blade loading, as these affect the acoustics. For motion, this examination will focus on the flap, lag, and elastic torsion at the blade tip as a function of azimuth angle. For loading, this examination will focus on the normal force coefficient multiplied by the Mach number squared ( $C_n M^2$ ) at a representative radial station (approximately  $0.88R$ ) as a function of azimuth angle. Most of the partners computed the blade motion and  $C_n M^2$  for the baseline case. Three partners provided blade motion and  $C_n M^2$  for the active twist cases.

The baseline (no active twist) blade tip flap motion—measured as the tip vertical displacement divided by the rotor radius and scaled by 100 for plotting purposes—is shown in Fig. 24. For this baseline case, three of the partners show a larger  $1p$  variation in flap motion than the other two.

For active twist cases, two partners predicted  $2p$  active twist would have the largest impact on BVISPL and one partner predicted  $3p$  active twist would have the largest

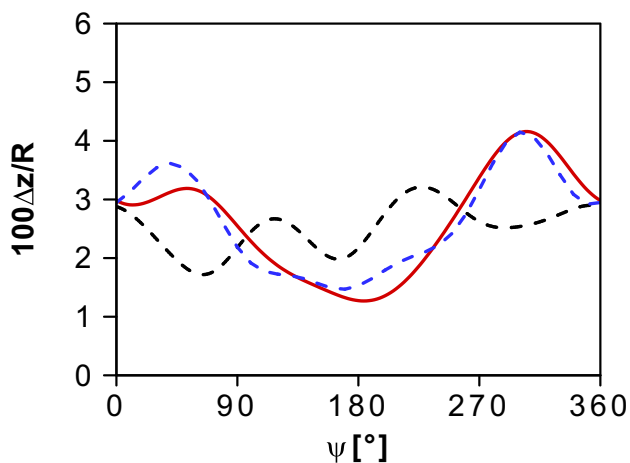


Fig. 25 Tip flap motion as a function of azimuth for active twist with best BVISPL reduction

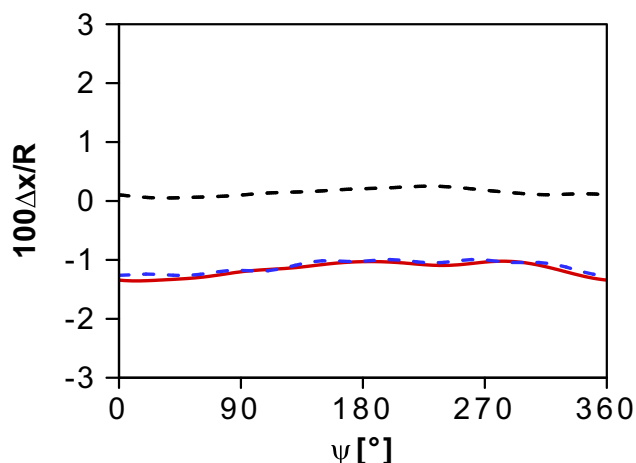


Fig. 27 Tip lag motion as a function of azimuth angle for active twist with best BVISPL reduction

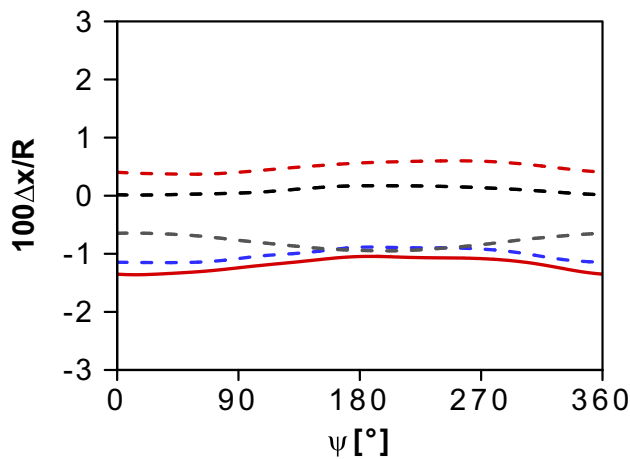


Fig. 26 Baseline tip lag motion as a function of azimuth angle

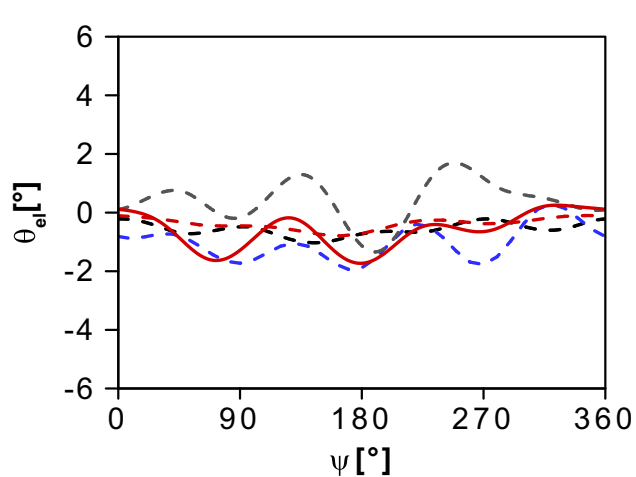


Fig. 28 Baseline elastic tip twist as a function of azimuth angle

impact on BVISPL. The tip flap motion for these “best BVISPL reduction” settings for each partner is shown in Fig. 25. Predictions from the two partners who used  $2p$  active show similar tip flap motion to that seen in their baseline results. Predictions from the partner who used  $3p$  active show a  $3p$  tip flap motion that is not seen in their baseline results. Similar to the tip flap motion discussed above, baseline lag motion is also divided by the rotor radius and multiplied by 100 for plotting purposes.

In Fig. 26, there is an appearance of a large discrepancy between partners’ predictions for the mean blade tip lag. However, the largest difference between all results is approximately  $1^\circ$  of lag motion measured at the tip. Also, the results do not show a large variation in lag as a function of azimuth. This appears to indicate that there are differences in the drag modeling for each partner because

mean drag on the blade will tend to result in a constant lag as seen in the figure.

Figure 27 also indicates that active twist does not have a profound influence on the lag motion of the blade. As seen in the previous figure, the mean lag offset between partners is probably due to differences in some aspects of modeling drag.

Figure 28 shows the baseline elastic tip twist as a function of azimuth angle. All predictions show an elastic twist bounded between  $-2^\circ$  and  $2^\circ$ , with individual predictions showing less peak-to-peak elastic twist than approximately  $3^\circ$ . Most predictions show a  $3p$  variation. This  $3p$  variation is consistent with the first torsion natural frequency of the blade being near  $3p$ .

Figure 29 shows the elastic tip twist with an active twist for these “best BVISPL reduction” settings for each partner.

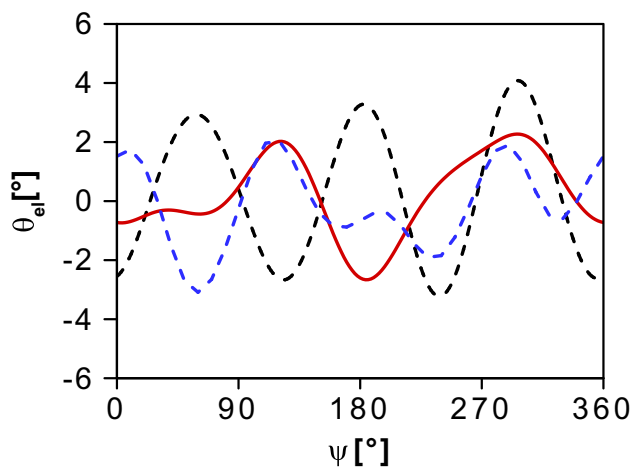
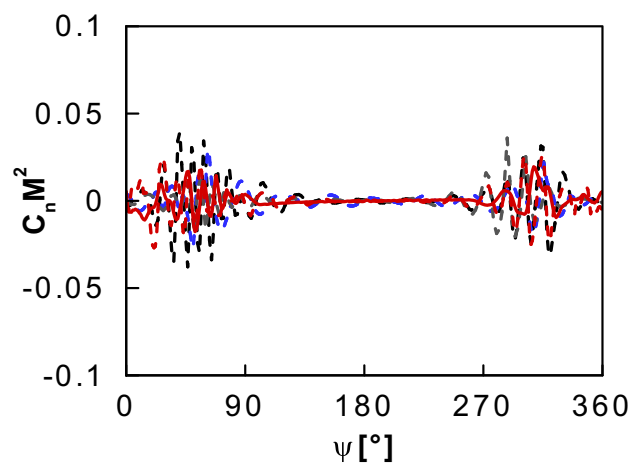


**Fig. 29** Elastic tip twist as a function of azimuth angle for active twist with best BVISPL reduction

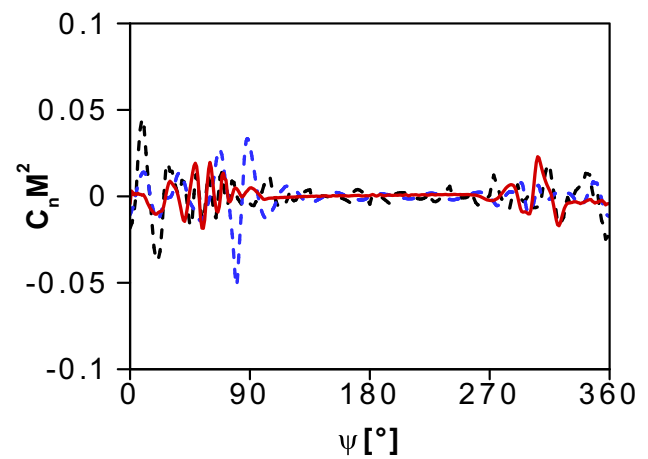
The peak-to-peak elastic twist for these cases is approximately double that of the baseline case.

Figure 30 shows the baseline blade normal force coefficient multiplied by the local Mach number squared ( $C_n M^2$ ) at a radial station of approximately  $r/R = 0.88$ , filtered to show only the 6th through the 40th (“mid-frequency”) BPF. This frequency range emphasizes the locations of BVI on the advancing and retreating sides of the rotor. All predictions indicate similar locations of BVI events on the advancing and retreating side of the rotor, but the magnitude of these events varies between partners’ results.

Figure 31 shows the mid-frequency  $C_n M^2$  with an active twist. The effects of active twist for these cases are primarily to change the magnitude and number of the BVI events and to move the BVI interaction locations.



**Fig. 30** Baseline mid-frequency  $C_n M^2$  as a function of azimuth angle



**Fig. 31** Mid-frequency  $C_n M^2$  as a function of azimuth angle for active twist with best BVISPL reduction

## 6 High speed: power, vibration, and HSI noise

A level flight condition with moderate blade loading  $C_T/\sigma = 0.0651$  was chosen at high advance ratio  $\mu = 0.349$  and  $\alpha_S = -11.1^\circ$  (nose-down) shaft tilt. Therefore, part of the rotor thrust is converted to propulsive force and needs to be accounted for in lift-to-drag ratio calculations. The blades encountered compressibility effects and retreating blade stall, leading to vibration and high-speed Impulsive (HSI) noise. The goal of the active twist application in this flight condition is to reduce vibration, noise emissions, and rotor power.

The trim goal was to match a fixed thrust coefficient with zero rotor rolling and pitching moments. Aeroelastic rotor simulations were conducted for the original blade and for a  $2p$  actuation with a control phase of  $210^\circ$  and 50% active twist amplitude. This type of actuation has been shown to improve rotor efficiency during initial simulations using comprehensive tools. DLR-CFD, KARI, KARI-CFD, and UofG provided the  $210^\circ$  phase result, while US, DLR-CA, and JAXA provided active twist phase sweeps in  $30^\circ$  increments. For the CFD results, KARI-CFD used an unstructured mesh of 28 M nodes, while structured grids were used by DLR-CFD, JAXA, and UofG with 33 M, 15.8 M, and 36 M cells, respectively.

The sum of the collective angle and the elastic tip deformation, averaged over one revolution, is shown in Fig. 32. The straight lines represent the results of the unactuated rotor blades, while the symbols show the value at the  $2p$  actuation cases versus the actuation phase. There is some spread in the baseline trim values. The CFD solutions of DLR and UofG show a grouping around  $9.8^\circ$ . The JAXA results and the active twist case of KARI-CFD are situated at a higher average collective. The combined collective and tip

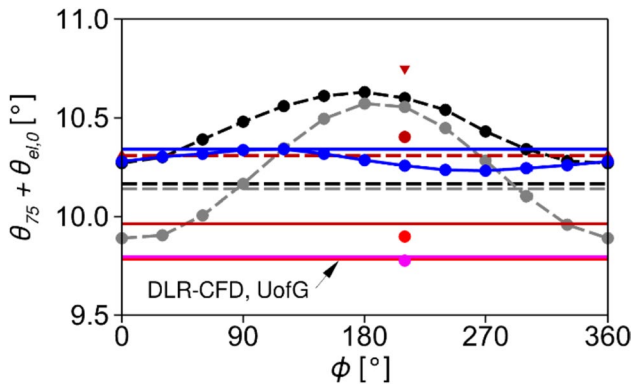


Fig. 32 Collective angle corrected for average tip torsional elastic deformation for baseline (horizontal line) and 2p actuation cases

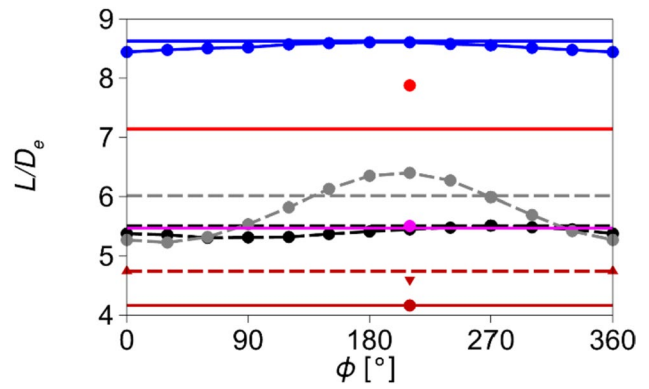


Fig. 34 Lift-to-drag equivalent for baseline (horizontal lines), 1p (DLR-CA only) and 2p twist actuation

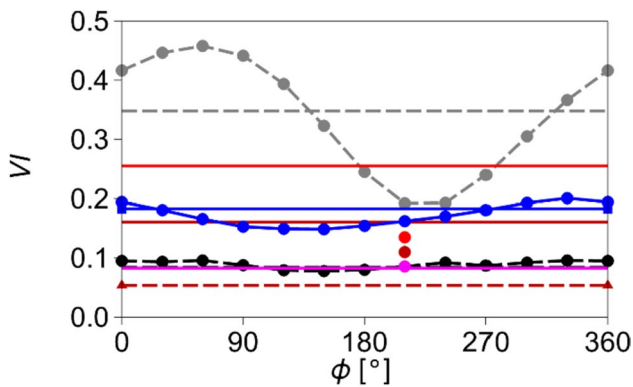


Fig. 33 Vibration index results for baseline (horizontal line), 1p (DLR-CA only) and 2p twist actuation

deformation angle for the 210° active twist case are around the baseline value or higher for all but the JAXA results.

The required longitudinal cyclic control angle decreased at 90° and increased at 270° active twist phase. The lateral cyclic control angle of the phase sweeps was at its highest at around 180°. A 210° phase shows a reduced or equal vibration Index (VI) compared to the passive rotor, but the scatter of the baseline VI is large, as shown in Fig. 33. JAXA-CFD, UofG, and US-CA predicted a power reduction with 210° active twist, while others showed an equal or higher value than the baseline and increased power at other phases.

Accounting for the change in trim state when active twist is applied, most codes predicted a higher propulsive force. A lift-to-drag equivalent value  $L/D_e$ , to include the horizontal force (defined positive downstream), is calculated by Eq. (4):

$$L/D_e = \frac{C_L}{C_X + C_Q/\mu} \quad (4)$$

The  $L/D_e$  is shown in Fig. 34. The trend is toward an equal or slightly lowered efficiency with an active twist.

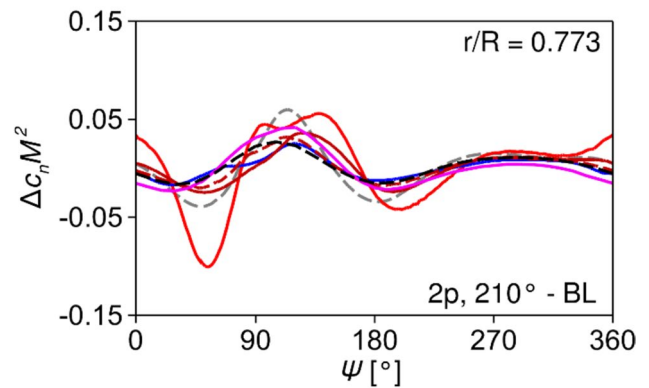
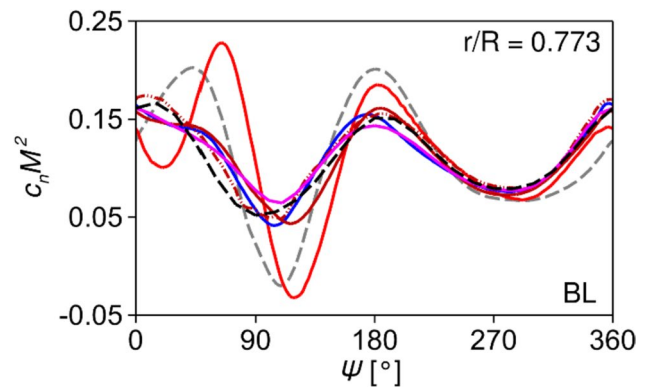


Fig. 35 Normal force coefficient at 0.773R for reference blade (top) and the difference between 210° active twist to reference (bottom)

However, DLR-CA simulations predict a significant increase. The 2p phase sweep showed reduced vibration and increased  $L/D_e$  at the same phase, with a direct impact on control angles. It also showed insignificant changes in blade flapping.

Normal and chordwise forces and sectional moments were recorded for three outboard blade locations. Good code-to-code agreement was found. Figure 35 represents the normal force coefficient for the baseline and for the active

twist results. The higher force peaks predicted by the DLR codes on the baseline rotor are partially canceled by the active twist system, explaining the strong improvements in vibration and efficiency.

The chordwise force coefficient shows excellent agreement between all partners, as shown in Fig. 36. The active twist has a small effect but increases the negative peak at the retreating side due to the high pitch angle lift component.

The sectional moment coefficient is relatively unaffected by the active twist of  $2p$  and  $210^\circ$  phase, as shown in Fig. 37. It is mainly negative (pitch down) for most of the rotor disk, with a peak on the 2nd quadrant. While results of JAXA predict less moment in the first quadrant, the  $2p$  actuation produces a similarly small offset on the sectional moments. Outboard of 75% radius, the active twist increases the pitch-down moment slightly in the first quadrant and reduces it in the second.

The azimuthal flapping of the blade tip is shown in Fig. 38. The comprehensive codes and KARI-CFD predict a  $1p$ -dominated flapping motion, with peak deflection at the retreating side. The remaining CFD codes show different flapping motions, explaining the differences in the trim state. Some of the changes are due to the different blade dynamics models used.

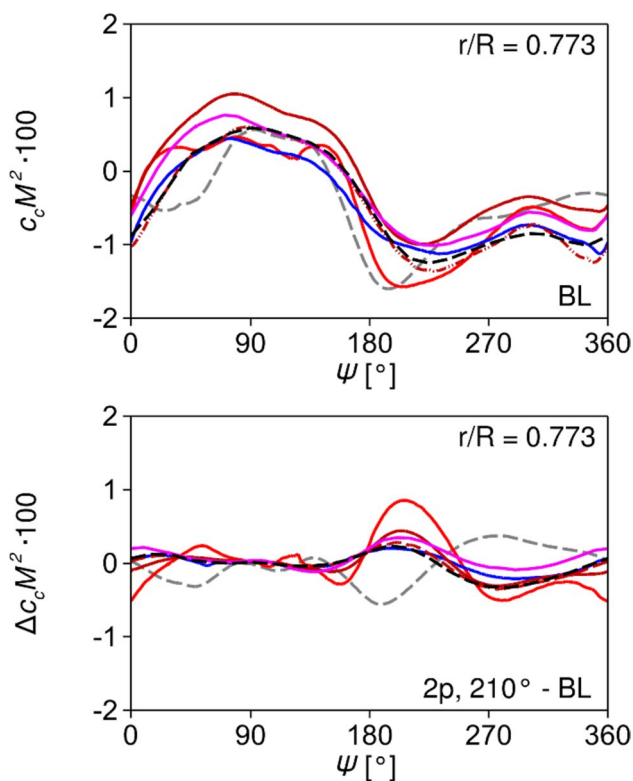


**Fig. 36** Chordwise force coefficient at  $0.773R$  for reference blade (top) and the difference between  $210^\circ$  active twist to reference (bottom)

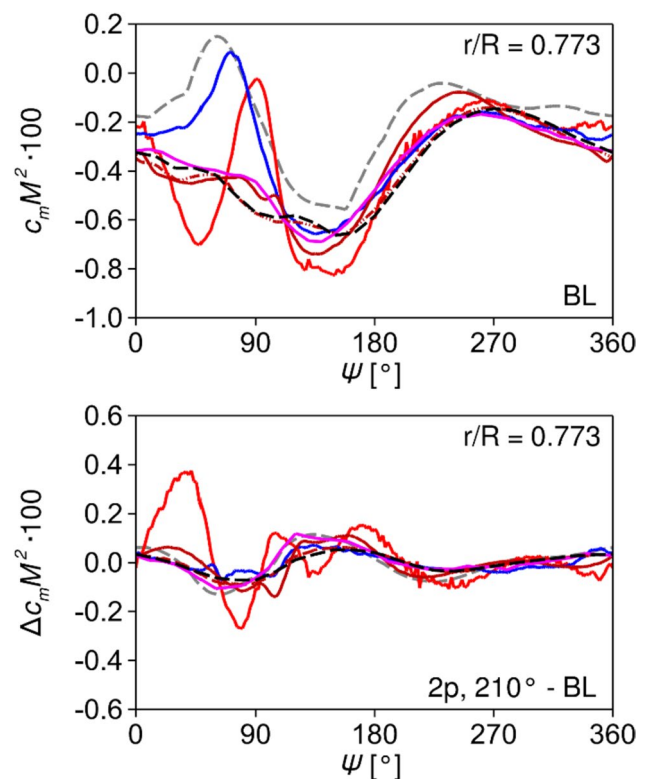


**Fig. 37** Sectional moment coefficient at  $0.773R$  for reference blade (top) and the difference between  $210^\circ$  active twist to reference (bottom)

The provided values of elastic blade tip torsion in Fig. 39 did not fully match the good correlation seen for the aerodynamic forces. DLR-CFD predicts the largest pitch-down tip twist at the advancing side. The active twist input correlates closely with the change in tip twist deformation, where the offset voltage and  $2p$  harmonic are clearly visible.

High-speed impulsive (HSI) noise radiation in the horizontal plane  $1.1R$  below the rotor is shown in Fig. 40. The peak noise level was recorded to be ahead of the advancing rotor blade, at a level slightly below the tip path plane on a  $1.5R$  sphere. The sound pressure level (SPL) did not vary significantly from 124 dB for the baseline rotor to 125 dB when the  $2p$   $210^\circ$  active twist was applied. The SPL obtained by JAXA in the horizontal plane  $1.1R$  below the rotor is shown for the baseline rotor,  $2p$   $180^\circ$  (min. noise) and  $2p$   $330^\circ$  (max. noise), showing a potential to reduce noise.

Concluding, with the trim goal of zero pitching and rolling moments, the propulsive force of the rotor was unconstrained. This did not allow a direct rotor power comparison, but the  $L/D_e$  ratio is comparable.

The  $2p$ ,  $210^\circ$  active twist showed some benefit in vibration index, at a similar rotor efficiency. DLR predicted larger force peaks, which were offset by the active twist system, showing the most promising vibration and efficiency

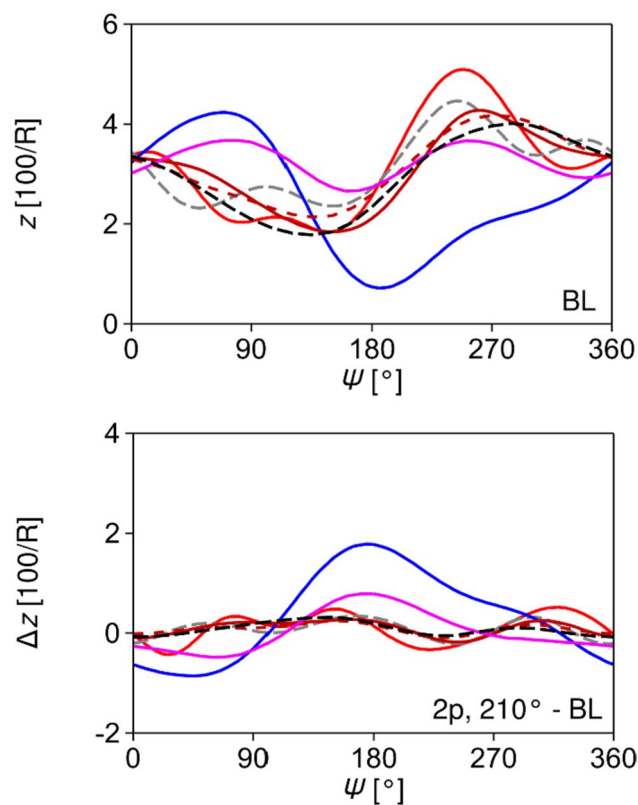


**Fig. 38** Blade tip flap deformation for reference blade (top) and the difference between 210° active twist to reference (bottom)

improvements. The change in collective angle from unactuated to actuated is linked to the static offset in the actuation, which is accounted for by adding the average tip twist angle to the collective. The harmonic active twist also affected the lateral and longitudinal cyclics.

Force correlations were matching well between partners, and the offsets produced by the active twist were consistent between codes. Larger differences are observed in the prediction of blade elastic deformations. The impact of the chosen active twist on the peak rotor noise direction was marginal.

## 7 High load: vortex-induced stall

The goal of this test condition is to investigate the dynamic stall phenomenon caused by the upwash of the preceding blade tip vortex on the rotor's retreating side. The potential to reduce the stall through active twist actuation will be explored. This flight condition occurs for a regular helicopter when highly loaded, for example, during maneuvering flight. That condition is therefore representative of the boundary of the operational envelope of a regular helicopter rotor.

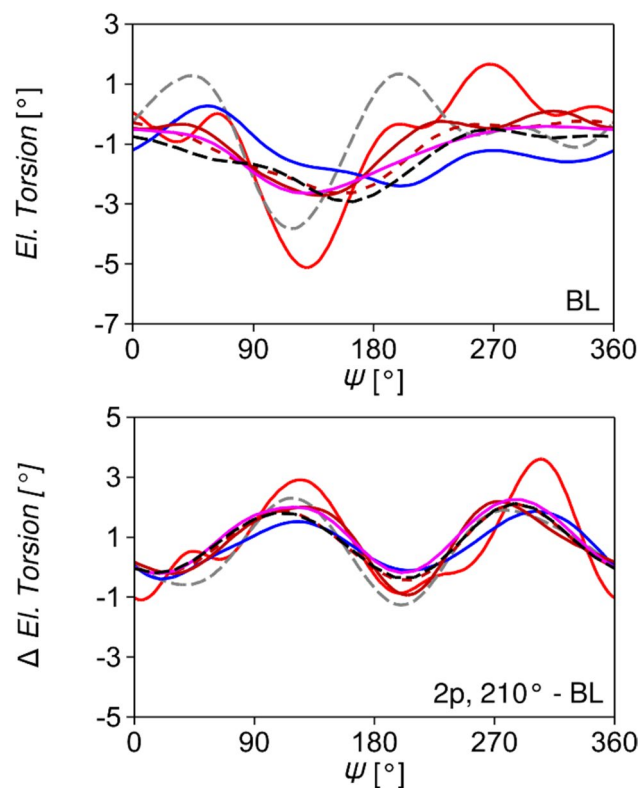


**Fig. 39** Blade tip torsion deformation for reference blade (top) and the difference between 210° active twist to reference (bottom)

The difficulty in mimicking this flight condition is that it is usually associated with a dynamic behavior such as a pull-up maneuver, which would be too difficult to replicate in the wind tunnel. For the general topic of dynamic stall, we refer the avid reader to the recent overview papers by Smith [63] and by Castells [64].

Initially, it was attempted to operate the rotor at nominal RPM and an advance ratio of  $\mu = 0.3$  in combination with a propulsive force trim, where the thrust would be gradually raised. However, multiple issues were encountered on this first attempt: First, the maximum thrust required to achieve a measurable stall was close to the limit of the rotor balance. Second, the power required was also close to the maximum power output of the motor. Additionally, a few partners predicted a strong aeroelastic coupling effect for the blade torsion exciting the second torsion eigenmode.

Thus, the flight condition has been altered to operate at half the nominal rotor RPM and wind tunnel speed to bring down the overall aerodynamic forces and moments. This roughly reduces the forces by a factor of 4 and reduces the required power by a factor of 8, therefore leaving an ample margin in power and scale limits. The loss of Mach scaling is considered acceptable because it is mostly a concern for the advancing blade side, where the phenomenon of interest does not occur. Additionally, the propulsive force trim is

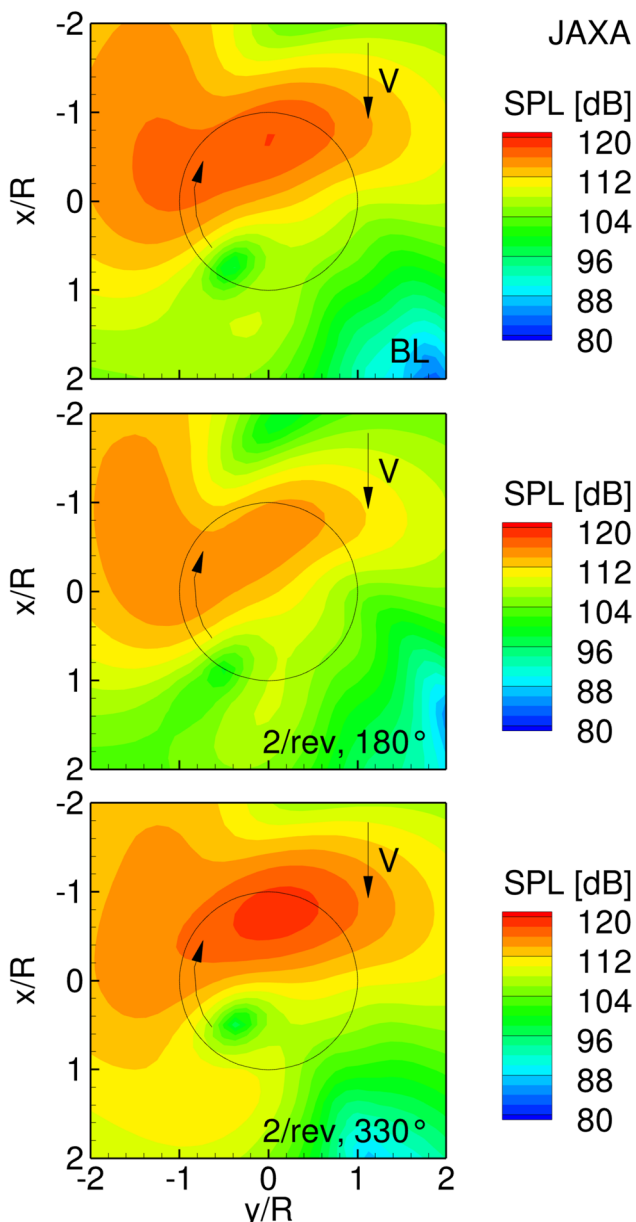


**Fig. 40** Noise level results of JAXA code in the horizontal plane 1.1R below the rotor hub for baseline (BL), minimum and maximum noise

changed to a zero-moment trim at zero shaft tilt  $\alpha_s = 0^\circ$ . In the first phase of this test case, the thrust is varied to find a common data point where most partners observe a stall. In the second phase, the actuation is applied to this common data point.

In Fig. 41, the control angles obtained by each partner for different blade loadings are reported. The simulations were run up to the maximum achievable thrust. Especially for the lower thrusts, a good agreement is observed, but with increasing thrust the results partially diverge. For example, the JAXA-CFD results predict a stronger rise in the magnitude of the control angles than the ONERA-CA results. Both

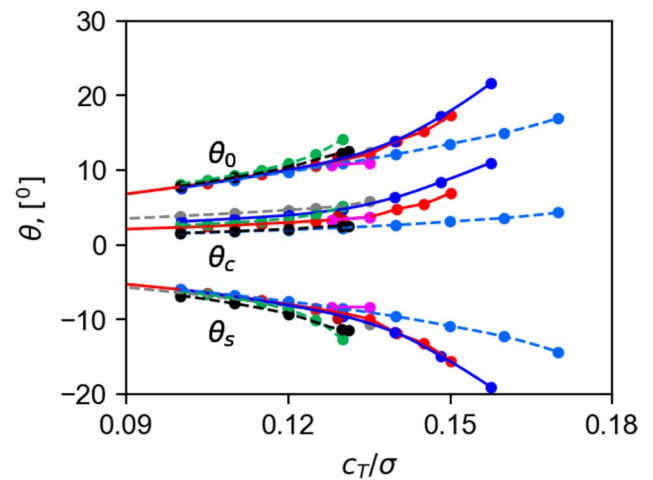


**Fig. 41** Control angles of the high-load condition

of these partners can converge their trim solutions at notably higher thrusts than the other partners.

Considering the data shown in Fig. 42, where the required power over thrust is plotted, a similar tendency as for the control angles is observed. For the lower thrust, a good agreement among the partners is found, while for higher thrust the results depart from each other. DLR-CA, DLR-CFD, KU-CA, and the JAXA-CFD results start with a linear trend that then curves upward as the stall onsets. However, the point at which this occurs is different for all of them. It is noteworthy that the ONERA results remain on a path of gradual increase until they are unable to trim the system anymore.

The vibration intrusion index, VI, is plotted as a function of thrust in Fig. 43. This metric shows even less agreement among the partners than the previous metrics and seems to be at very different levels. A commonality

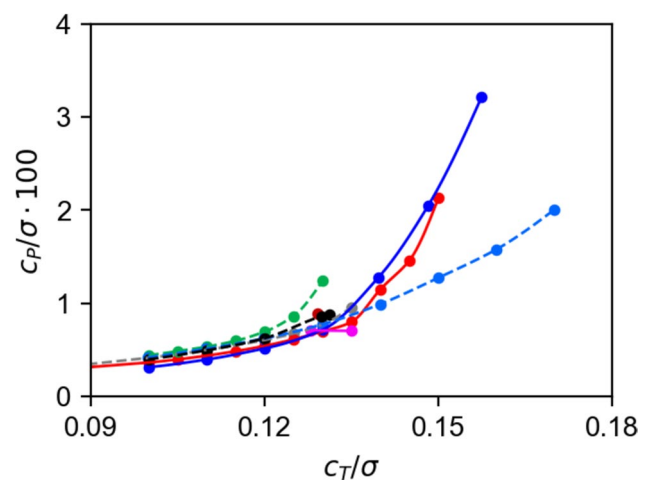


**Fig. 42** Power required, high-load condition

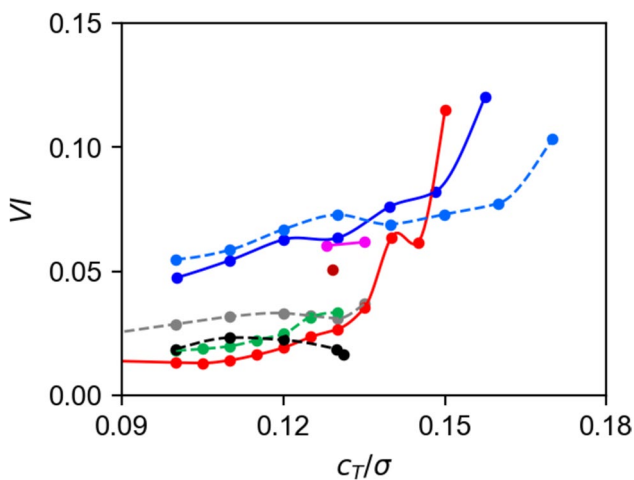


Fig. 43 Vibration intrusion index

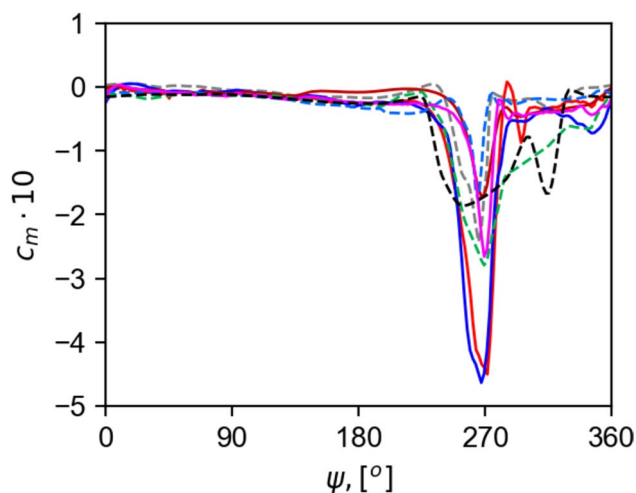


Fig. 45 Section moment coefficient,  $r/R = 0.67, C_T/\sigma = 0.13$

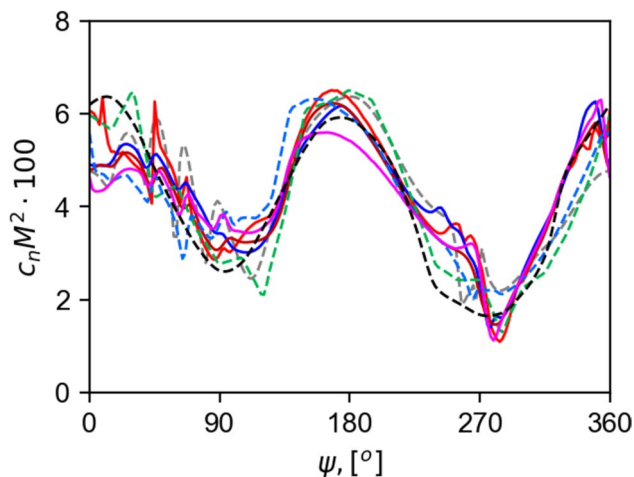


Fig. 44 Section normal load coefficient,  $r/R = 0.67, C_T/\sigma = 0.13$

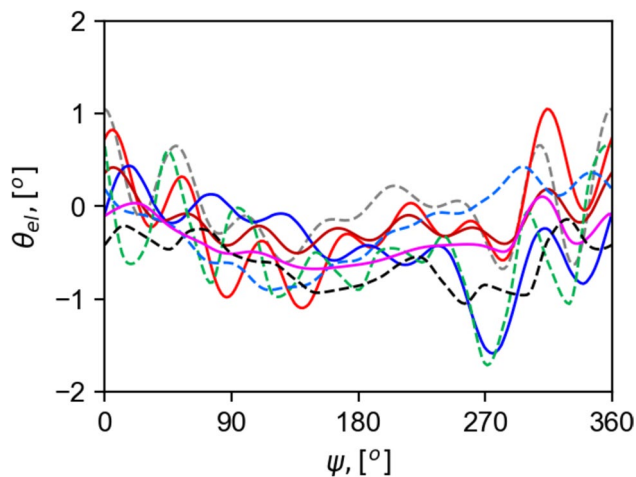


Fig. 46 Blade tip torsion,  $C_T/\sigma = 0.13$

observed for most partners is that with the onset of the stall (where the power consumption also increases), the vibration index rises. Additionally, for  $C_T/\sigma = 0.13$ , the CFD-based results arrive at a similar level, which may be coincidental given the otherwise very different behavior.

To analyze this matter in more detail, the sectional normal force and pitching moment are investigated for the spanwise section at  $r/R = 0.67$  in Figs. 44 and 45. This spanwise location will be the next closest instrumented section in the experiment to where the vortex of the previous blade passes on the retreating side. The chosen blade loading is  $C_T/\sigma = 0.13$  as it showed an onset of stall while still sufficiently far away from the maximum thrust to test the actuation. For the normal force in Fig. 44, a general  $2p$  trend is captured, yet the higher harmonic content caused by advancing and retreating side BVI is differently resolved by the partners. The US-CA result does not

capture any of it due to a  $15^\circ$  time step, whereas DLR-CFD has the most.

The pitching moment in Fig. 45 is very similar among the partners for the most part, but in the retreating to aft side of the rotor disc, the results show a noticeable spread. DLR-CFD and JAXA-CFD show a strong pitching moment indicating a deep stall, and a moderate stall is reported by the other codes.

The pitching moment is linked with the torsional deflection shown in Fig. 46. It is seen that if a severe stall is found in Fig. 45, a stronger excitation of the first torsion mode is found here as well. For DLR-CFD, the peak-to-peak value of  $2.2^\circ$  is the largest, while UofG-CFD with  $0.8^\circ$  is predicting the lowest range of torsion.

An additional concern of this test case is the blade flapping shown in Fig. 47, which remains in acceptable ranges and, therefore, will likely not be an issue during testing.

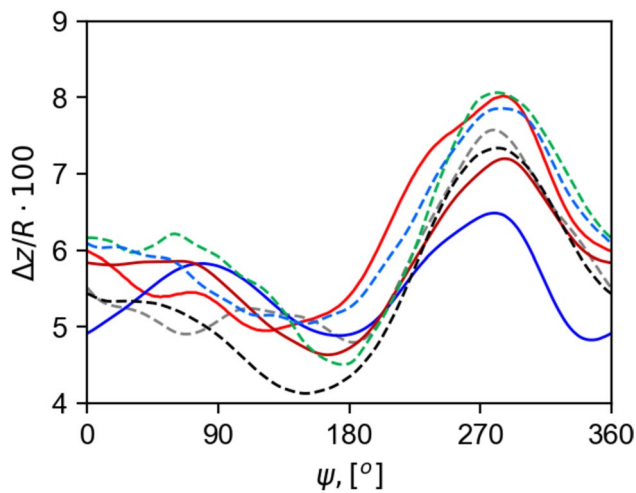


Fig. 47 Vertical blade tip deflection,  $C_T/\sigma = 0.13$

The intermediate conclusion from the first phase study of this case is that the ability to predict dynamic stall is a challenging task and likely requires a lot more resources to correctly predict. The CFD-based results are considered more reliable than the purely CA-based results due to their theoretical higher fidelity approach. In contrast to the applied prescribed and free-wake codes for the CA-based results, no simplifications regarding compressibility or viscous effects are made, nor do they rely on predetermined 2D data for airfoils. In order to capture this 3D event of the dynamic stall of a rotor, sophisticated simulation approaches are required; see Ref. [63]. While for DLR-CFD the stall occurs already at lower thrust levels, the severity of the stall becomes similar at higher thrust levels for JAXA-CFD. Therefore, it is believed that in the experiment, the exact thrust needs to be found.

To understand the overall flow physics better, the vorticity in the rotor system has been plotted for the CFD simulations at  $C_T/\sigma = 0.13$  in Fig. 48.

In all cases, the vortex traveling over the retreating side is resolved, yet at different strengths. DLR-CFD and JAXA-CFD resolve a stronger vortex than KARI-CFD and UofG-CFD, likely due to the application of a fourth-order inviscid flux scheme and a background grid spacing of  $\Delta x/c = 0.1$ . DLR-CFD resolves more secondary vortices being attributed to the application of DES over URANS. Linking these qualitative findings with Fig. 45, the stronger resolved vortex is therefore directly linked with the stronger pitching moment stall and DLR-CFD and JAXA-CFD obtain very similar results. UofG using a third-order inviscid flux scheme and an uneven grid spacing between  $\Delta x/c = 0.05$  to  $0.15$  shows a stronger pitching moment than KARI with a second-order inviscid flux scheme using an even spacing of  $\Delta x/c = 0.15$ .

A wide range of actuations has been investigated, from a steady  $0p$  and  $1p$  to  $5p$  actuations. Not all partners could run

all data points; however, DLR-CA, DLR-CFD, and ONERA-CA could provide the full set. To facilitate finding effective actuation settings, contour plots of the required power and vibration intrusion index have been prepared and are presented in Fig. 49. While discrepancies can be observed, the most beneficial actuation frequency is likely  $2p$  in terms of power and vibration reduction. Therefore, the remaining partners were encouraged to deliver results for this actuation frequency.

In Figs. 50 and 51, the required power and vibration intrusion index relative to the baseline value by the respective partners' results are plotted. Despite the attempt to normalize the results, the solutions are quite diverse. Nevertheless, a crude observation can be made: Using an aft-disk phase ( $\phi \approx 330^\circ\text{--}60^\circ$ ) reduces the required power for all partners, but the required power increases around the front-disk phases ( $\phi \approx 90^\circ\text{--}270^\circ$ ). Looking toward the vibration intrusion index results, they are more diverse than has already been shown for the baseline cases. Here, it seems that most, but not all partners, predict an improvement for phases  $\phi \approx 30^\circ\text{--}120^\circ$  and a deterioration for the retreating side phases  $\phi \approx 180^\circ\text{--}330^\circ$ . The current working assumption for the second prediction stage of this high-load investigation is that a phase of  $\phi = 0^\circ\text{--}90^\circ$  at  $2p$  will likely enable benefits in this flight condition and is worth considering in the wind tunnel experiment.

## 8 High advance ratio: $L/D$ ratio and vibration

The last test matrix scenario considered is a slowed rotor, high advance ratio (HA) flight. The rotor speed is reduced to 50% RPM at the wind speed of 76 m/s, resulting in an advance ratio of  $\mu = 0.7$ . The 50% reduction is chosen considering the previous slowed rotor test cases such as a full-scale UH-60A rotor [65]. The present HA condition simulates a high-speed compound helicopter or autogyro configuration of a rotor. The RPM reduction leads to a large increase in the reversed flow region. Trimming the rotor to zero rolling moment results in a significant region of negative lift on the advancing blade tip. This negative lift region results in a high differential aerodynamic loading over the advancing side of the rotor disk. The slowed rotor also drives a large blade flapping due to the decreased centrifugal action and lower loads acting over the blade. Furthermore, the blade natural modes upshift to higher frequency zones (e.g., the first torsion mode shifts from  $3.78p$  to  $6.97p$ ). All these features make the HA condition quite challenging from both the aerodynamic and the aeroelastic viewpoints.

The goals of the current HA task are set to confirm: first, the prediction capability in capturing the essential aeromechanics phenomena of the slowed rotor (HA1) and,

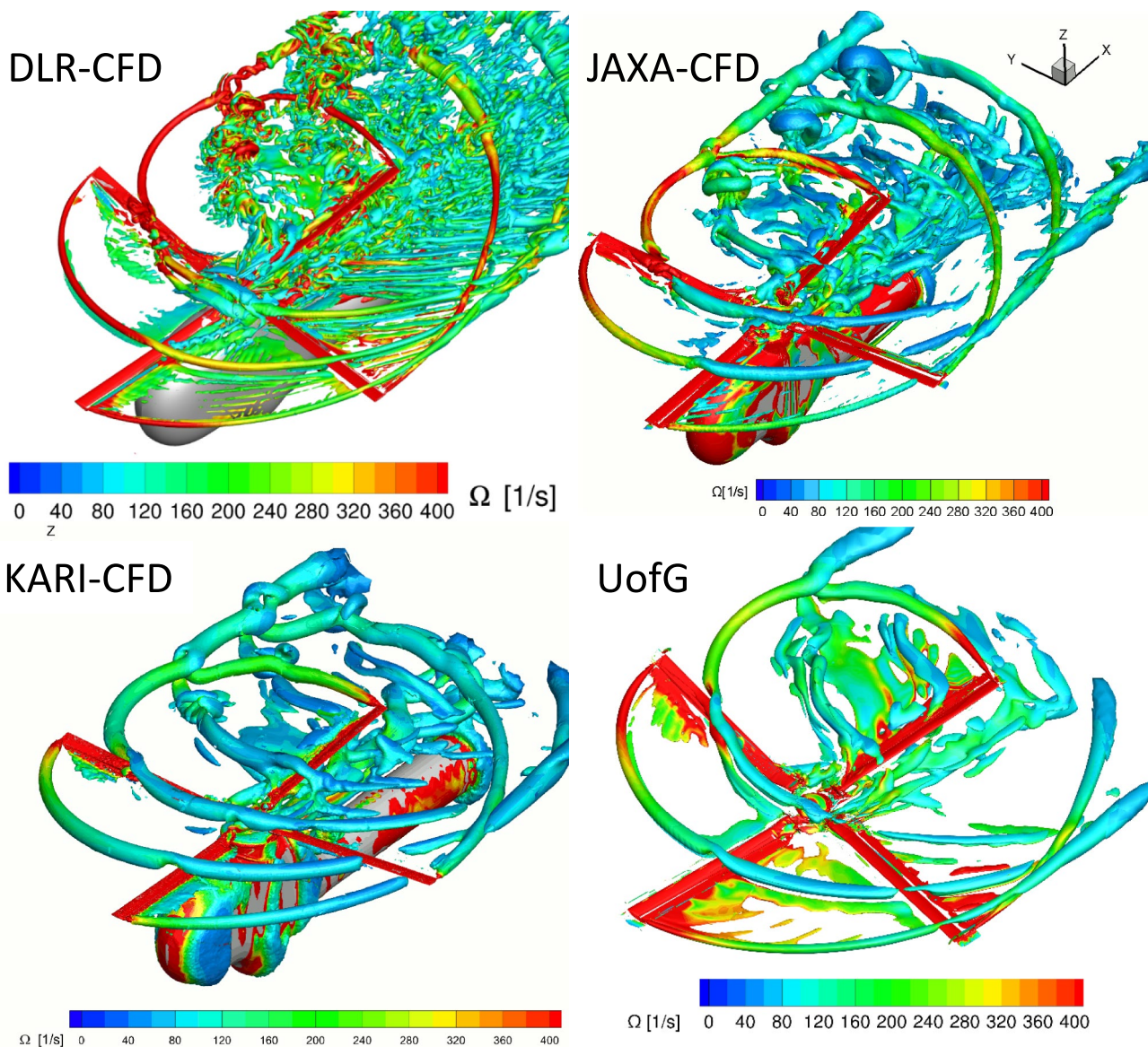


Fig. 48 Vorticity plots, Q-criterion ( $10^3 \text{ 1/s}^2$ )

second, the benefits in association with the hub vibration and performance aspect exploiting the active twist authority (HA2). The HA1 condition is an unactuated slowed rotor test that has been studied previously in the literature [65], while the HA2 case is unique in this work. It is noted that the STAR HA condition utilizes a limited set of test points, as compared with the wide coverage of the test matrix in the UH-60A test campaign [65]. For instance, the collective angle and rotor RPM are kept constant with shaft angles varied from  $-4^\circ$  to  $+4^\circ$  in the STAR HA condition, whereas in the UH-60A slowed rotor test, both the collective ( $-0.1^\circ$  to  $+8^\circ$ ) and rotor RPM (65%, 40%) are varied as a function of shaft angles ( $0^\circ$ ,  $+4^\circ$ ). This reduced test set is used to focus on special features of the slowed

rotor while exploiting the twist actuation gains, under the strict budget and time constraints.

In the HA1 case, a trim to zero hub moments is used to determine the cyclic control angles with the collective pitch fixed at  $\theta_0 = 4^\circ$ . Figure 52 shows the comparison of predicted trim control angles with shaft angle variations. An apparent linear response of the trim control angles with shaft angle changes is predicted reasonably among the different approaches, with slight deviations in amplitudes (less than  $1^\circ$ ). The calculated thrust values ( $C_T/\sigma$ ) indicate a monotonic increase with shaft angles (not shown), as observed in the UH-60A slowed rotor test [65]. This close correlation among the predicted results assures the

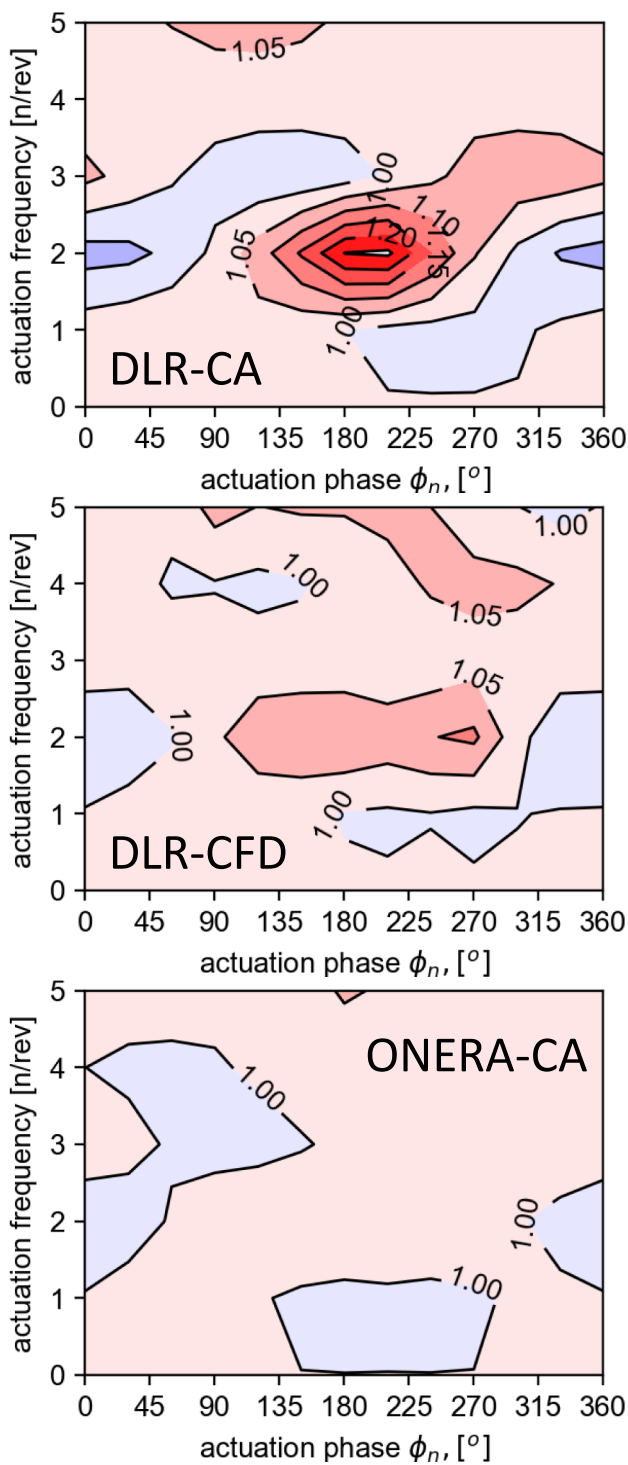


Fig. 49 Relative required power for various actuation settings; iso-lines are incremented by 0.05

consistency of the analysis methods with confidence in the trim convergence set for the HA condition.

Figures 53 and 54 illustrate the comparison of results obtained for section normal force and pitching moment coefficients in the time domain, respectively, predicted

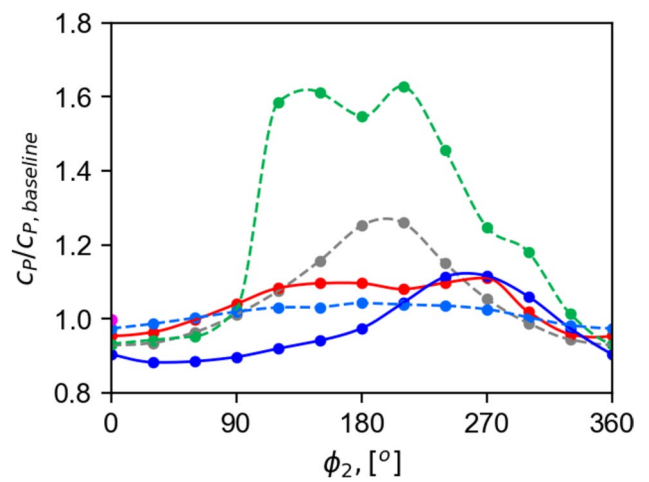


Fig. 50 Relative power required,  $C_T/\sigma = 0.13$ , 2p phase sweep

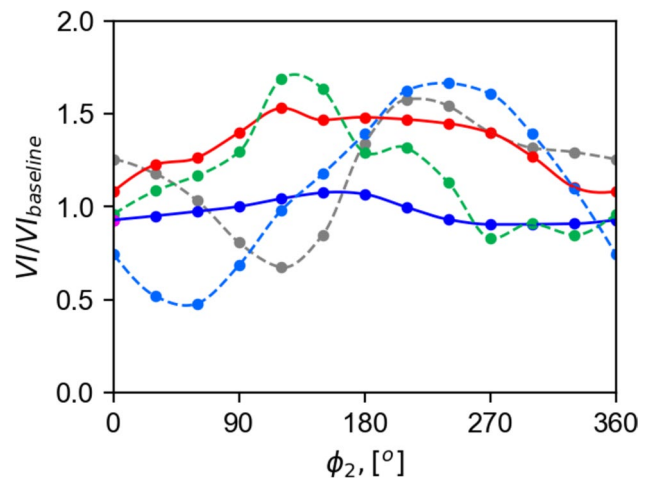


Fig. 51 Vibration intrusion index,  $C_T/\sigma = 0.13$ , 2p phase sweep

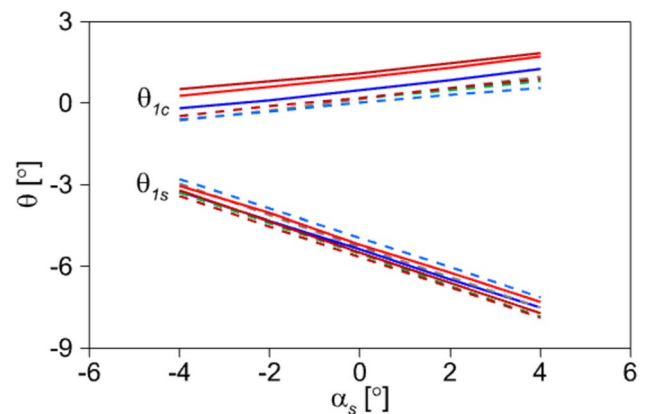


Fig. 52 Comparison of trim control angles with shaft angle changes

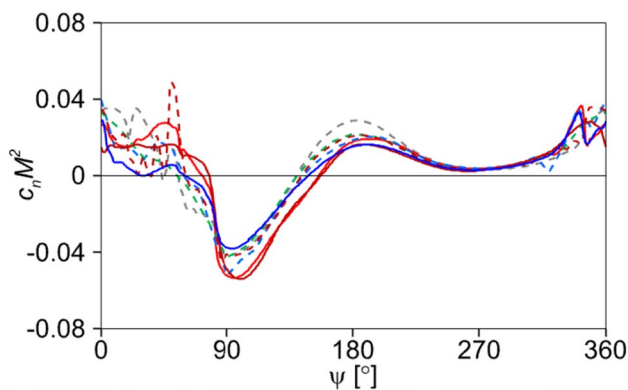


Fig. 53 Comparison of the section normal force coefficients at  $r/R = 0.875$  ( $\alpha_s = 0^\circ$ )

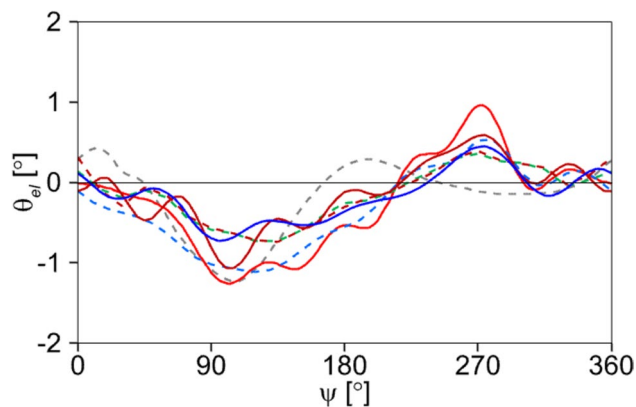


Fig. 55 Comparison of tip elastic twist deformation ( $\alpha_s = 0^\circ$ )

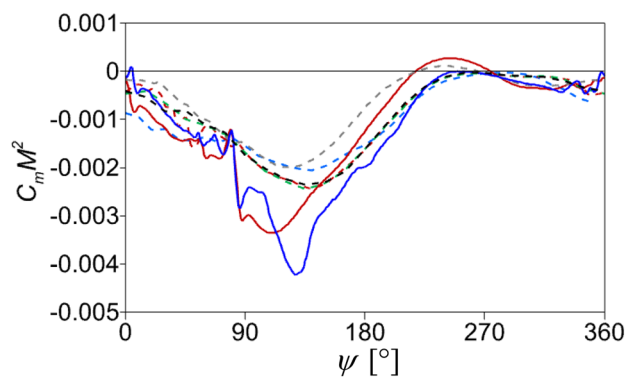


Fig. 54 Comparison of the section pitching moment coefficients at  $r/R = 0.875$  ( $\alpha_s = 0^\circ$ )

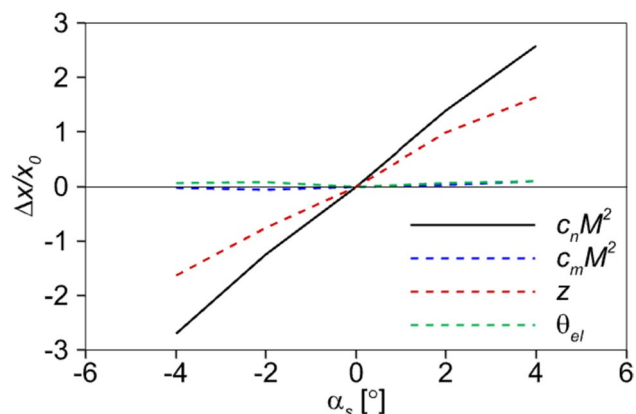


Fig. 56 Effect of shaft angles on section airloads and blade deformation (reference value at  $\alpha_s = 0^\circ$ )

at the radial station of  $r/R = 0.875$  with a shaft angle of  $\alpha_s = 0^\circ$ . Good agreements appear to be obtained in terms of the waveform and peak-to-peak magnitudes among the diverse set of signals that include CSD alone (dashed lines) and CFD/CSD coupled (continuous lines) results. It is indicated that the dominant phase response of the section normal forces signal is predicted to be nearly equivalent by all methods.

For both section normal force and pitching moment signals, CFD/CSD predictions show larger negative peaks around  $90^\circ$  azimuth angles and more oscillatory signals (i.e., indication of BVI events) in the first and fourth quadrants of the disk than those by CSD alone methods. It is observed that the dominant phase response of the section airload signal is predicted almost the same behavior by all methods. The large negative peak in the outboard region of the advancing side is expected as the reversed flow regime occupies a substantial portion of the opposite side at  $\mu = 0.7$ , which leads to high differential airloading over the advancing blades. This trend is better captured in the section pitching moment signals predicted using the first

principle-based CFD/CSD methods with much finer grids, as shown in Fig. 53.

Figure 55 shows the comparison of elastic twist deformation at the blade tip when  $\alpha_s = 0^\circ$ . Though the local response shows substantial scatter among the results, the general trend (nose-down on the advancing side and nose-up on the retreating side) is captured reasonably by the analyses. As can be seen, a highly oscillatory pattern close to  $7p$  is obtained, particularly in CFD/CSD predictions.

The prominent  $7p$  signal is essentially augmented by the first torsion blade natural frequency shifted by the reduced RPM and is responsible for generating the differential air loading pattern found in the section normal forces (Fig. 53) through the mechanism of the trim. It is seen that most CSD predictions except DLR-CA capture the low-frequency waveform of CFD/CSD results while showing some of  $7p$  oscillatory behavior.

Figure 56 presents the influence of shaft angles on section airloads ( $C_n M^2, C_m M^2$ ) and blade elastic deformations ( $z, \theta_{el}$ ). For relative comparison, the mean values of all

predicted results are averaged and presented in % values, with the reference set at the mean of  $0^\circ$  shaft angles ( $x_0$ ). It is indicated that both, section normal force coefficients and tip flap deflections, increase with shaft angle changes while the mean of either section pitching moments or tip elastic twist deformation remains nearly unchanged. This outcome is consistent with the predicted thrust trends though not shown explicitly.

The predicted rotor power (induced plus profile power) is shown in Fig. 57 versus  $\alpha_s$  changes. As discussed above (Fig. 52), the required power in HA condition is expected to be very small due to the trim setup, which may fall within the measurement error of the wind tunnel test capacity (190 kW). Nevertheless, all the predicted results pick up the general up-down trends as shaft angle changes, with upper bounds by KARI-CFD results. The reason for overprediction in KARI-CFD is likely due to its consideration of a blade inboard shank model that has been neglected by other analyses.

Figure 58 shows the comparison of equivalent lift-to-drag ratios ( $L/D_e$ ) with respect to shaft angles. The general trends in  $L/D_e$  with shaft angles are captured by the analyses but with wide scatter in amplitudes. The upper and lower bound results are obtained by DLR-CA and KARI-CFD, respectively. The shank model incorporated in the KARI-CFD analysis apparently contributes to underestimate  $L/D_e$  predictions relative to the others.

Next, the actuation scenarios (HA2) for the minimum vibration and/or the best performance are sought through the application of active twist control. Retrim to the thrust values and hub moments of the corresponding nonactuated cases with the shaft axis fixed at  $\alpha_s = 0^\circ$  is applied to examine the active twist gains. The actuation cases include steady voltage and dynamic frequency sweeps with the variations in actuation voltages (amplitudes) and phase angles.

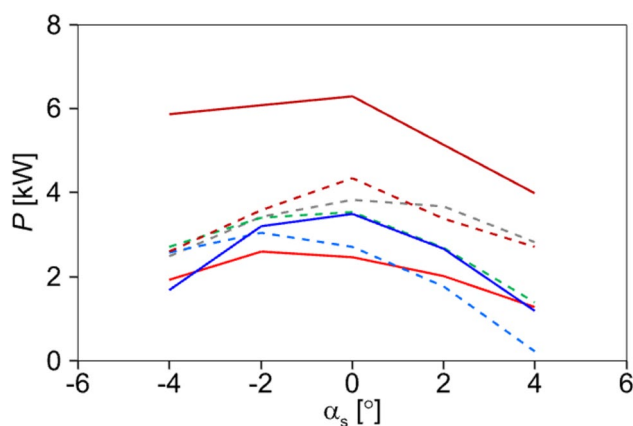


Fig. 57 Effect of shaft angles on rotor power

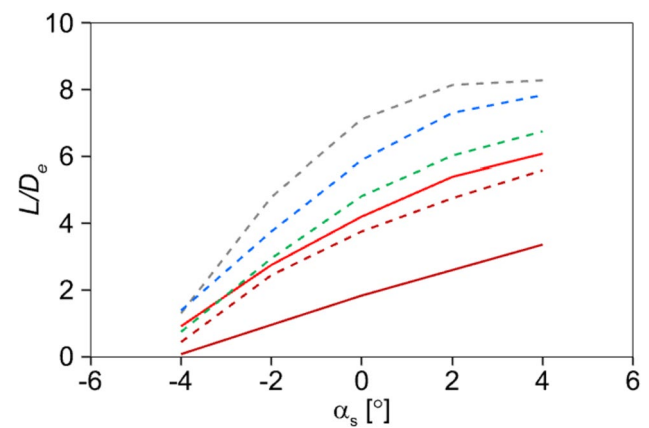


Fig. 58 Effect of shaft angles on rotor  $L/D_e$

Figure 59 shows the effect of applying steady  $0p$  voltages ( $U_0$ ) on the vibration intrusion index (VI) defined in Eq. (2), for the rotor in high- $\mu$  flight. The actuation voltages are varied from  $U_0 = -500$  V to 800 V with an offset of 400 V. Only the predicted results with CA methods are presented in the comparison. It is indicated that most results estimate increased vibration reductions with higher voltages, with maximum gains obtained at 800 V. Up to 38% reduction referenced to the baseline cases is shown with the steady actuation.

The voltage sweep behavior is also studied for rotor power and  $L/D_e$ . It is observed that most predicted results indicate increases in  $L/D_e$  at or over 250 V, while no significant changes in rotor power are found among the predictions. The increased gains in  $L/D_e$  are up to 2.7% (not shown). The favorable zones with possible improvements in  $L/D_e$  are indicated in Fig. 59 in the yellow box. In summary, both the vibration reduction and performance ( $L/D_e$ ) improvement are feasible with an active twist control technologies, without incurring significant power penalty.

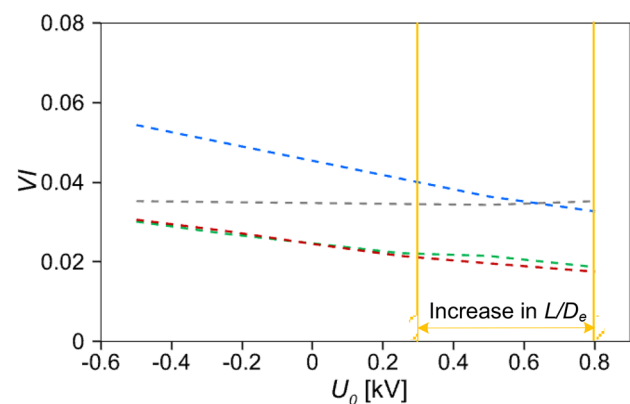
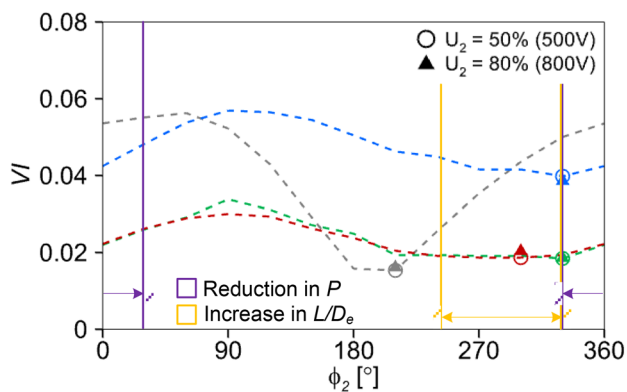


Fig. 59 Effect of voltage sweep on VI at steady  $0p$  actuation and 400 V offset



**Fig. 60** Effect of phase sweep on VI at dynamic  $2p$  actuation ( $U_2 = 500$  V) and 400 V offset

A  $2p$  actuation is investigated also for performance and vibration behavior of the rotor in high  $\mu$  flight. Figure 60 shows the phase sweep response of the group simulation results on VI at the dynamic voltage of  $U_2 = 500$  V and with 400 V offset. It is observed that the phase sweep has a great potential in reducing hub vibrations, with substantial deviations among the predicted results. Most predictions (KU, KARI, and ONERA) show almost the same waveform in the phase response, with apparent offset by ONERA results.

The open circles in Fig. 60 indicate the best phase angles that could result in a minimum hub vibration. The maximum gain is estimated by DLR-CA, with the percentage values of about 55% based on the unactuated case. It is observed that the phase angle of  $330^\circ$  appears to be one of the best conditions for minimum VI at  $2p$  frequency input. Another attempt is made to see whether an increase in voltage levels to 800 V can contribute further to reduce the hub vibration, based on the predicted minimum VI locations at 500 V input.

The solid triangles in Fig. 60 denote the results with 800 V actuation. Most results (except ONERA) indicate an increase in VI with the increased voltages. This signifies that the vibration reduction gain is nonlinear in response to the voltage input. It is concluded that a 500 V input is recommended as the best scenario for the active twist input in a high  $\mu$  condition.

In Fig. 60, the predicted zones of possible improvements in  $L/D_e$  and reductions in rotor power are indicated in yellow and purple color, respectively. The maximum gains are predicted to be: 2.9% reduction in rotor power and 2.0% improvement in  $L/D_e$ . Though the performance gain is limited (less than 3%), it is likely to meet the best actuation condition, by concurrently reducing VI and improving  $L/D_e$  with decreases in required rotor power, when the phase angle is set at  $330^\circ$  with  $2p$ , 500 V active twist input.

So far, the simulation is conducted with the collective angle fixed at  $4^\circ$ . In this collective setting, both rotor power and hub vibration levels remain relatively low as observed

above. The earlier HA rotor test on the UH-60A rotor [65] covers a broader range of collective control angles ( $0^\circ$  to  $8^\circ$ ) at  $\alpha_s = 0^\circ$ . The preliminary investigation shows that the predicted thrust falls within the test envelope of the full-scale UH-60A rotor. The influence with an increase in collective angles is studied at the shaft angle of  $0^\circ$ . The collective settings are varied from  $4^\circ$  to  $8^\circ$  with an interval of  $2^\circ$  while maintaining the zero-moment trim strategy.

Figure 61 shows the percentage changes in the rotor performance and hub vibration, as the rotor collective angle varies. The percentage values are obtained based on the results of the  $4^\circ$  case. Each bar in the plot represents the simple average of the partners' results for each of the parameters (e.g., VI,  $L/D_e$ ). As can be seen from the plot, substantial gains in the respective magnitudes are obtained with higher collective angles. For instance, VI is increased by 43.6% at  $\theta_{75} = 8^\circ$  as a reference to  $4^\circ$  case. With the elevated levels, it appears to have a greater potential to reduce vibration and improve rotor performance through the ATR scheme in HA flight regime.

The collective sweep response on VI as a function of actuation voltages is studied next. Figure 62 shows the influence of steady  $0p$  actuation on rotor hub vibration. All partners' results are averaged to capture the trend clearly. As expected, VI increases significantly (about 30%) as the collective angle varies from  $4^\circ$  to  $8^\circ$ . It indicates that the vibration is decreased with increased voltage inputs due to the untwisting response of the blade. However, the slopes reduce, showing less sensitivity, with increasing collective control angle.

Figure 63 presents the comparison of hub vibration levels predicted when dynamic  $2p$  actuation ( $U_2 = 500V$ ) is used, as functions of actuation phase angles at the collective angle of  $8^\circ$ . The phase behavior is similar to the previous results shown in Fig. 60, with apparent increase in amplitudes. Most CSD predictions (except DLR S4) estimate a

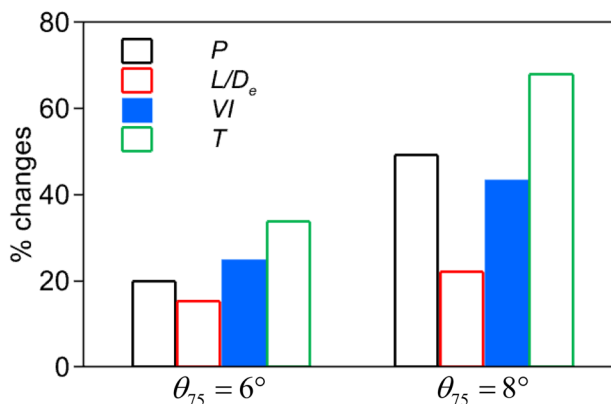


**Fig. 61** Effect of collective sweep on rotor performance and vibration measures

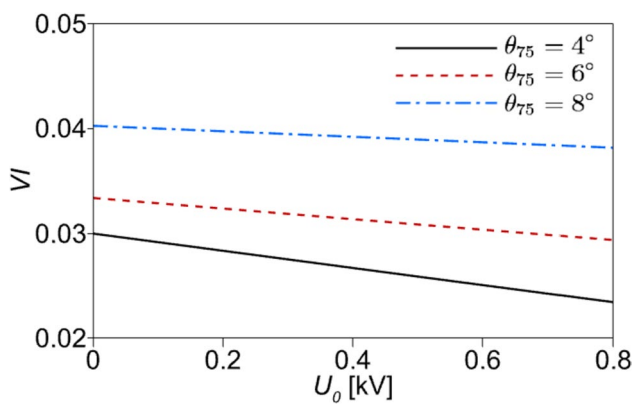


**Fig. 62** Effect of voltage sweep on VI at steady  $0p$  actuation and 400V offset, with varying collective angles

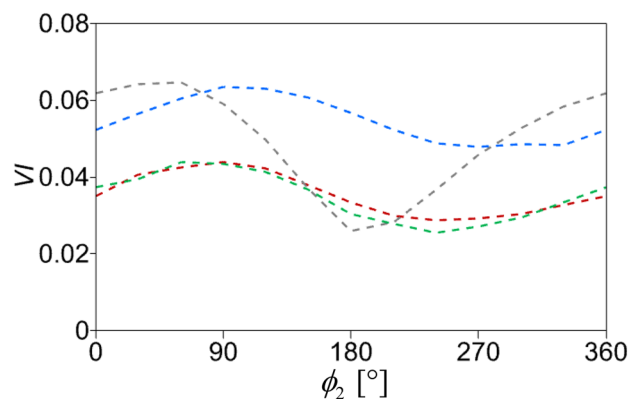


**Fig. 63** Effect of phase sweep on VI at dynamic  $2p$  actuation ( $U_2 = 500V$ ) and 400V offset, with the collective angle of  $8^\circ$

minimum vibration around the phase angle of  $240^\circ$ , with 22.4% reductions in absolute values. Though not shown explicitly, further results on rotor power consumption and performance measure ( $L/D_e$ ) with respect to the collective angles are produced to examine the potential benefits of ATR in high  $\mu$  flight.

## 9 Conclusions

The predictions show the following:

- The achievable improvement of hover figure of merit is rather small, because the available steady active twist of approximately  $2^\circ$  is much smaller than needed.
- In low-speed descent, the BVI noise and vibration reduction by active twist are comparable to that obtained by HHC or IBC.

- In high-speed flight, the power gains due to active twist are comparable to those obtainable by IBC.
- The numerical prediction of the vortex-induced (deep) stall condition at high load is very challenging. Good potential to either reduce the required power or the vibration is foreseen, but results vary due to noticeable differences in the predictions. A reduction of the RPM to 50% of the nominal RPM will likely enable safe operations in the wind tunnel.
- The predictions at high  $\mu$  with reduced RPM indicated reasonable agreements among the group simulation results. Both steady  $0p$  and dynamic  $2p$  actuation showed significant vibration reduction gains relative to unactuated cases. The amplitude or phase sweep study revealed that the best actuation condition could be met at  $2p$  and 500 V input with  $330^\circ$  phase angle, for concurrent reduction in hub vibration and rotor power while improving rotor  $L/D_e$ .
- The variety of trends observed reveals that even with the current state-of-the-art computer codes, a sufficient agreement of results prior to the wind tunnel test cannot be found in all of the operational conditions.
- Despite this, the predictions give very valuable insight to the test team for setting up the test matrix to focus on the most promising conditions and make the best use of the available wind tunnel time.

**Author contributions** The contributions to this manuscript were shared in the following manner: BGW: Responsible for the overall compilation, Abstract, List of symbols, Sects. 1, 3, 3.1, 3.2.1, 9; Contributions to Sects. 4, 5, 6, 7, 8. JR, SK: Sect. 2. GW: Responsible for Sects. 7, 3.2.2; Contributions to Sections 4, 5, 6, 7, 8. JWL, DDB: Responsible for Sect. 5. Contributions to Sects. 3.2.4, 4, 5, 6, 7, 8. JB, YD, IC: Responsible for Sect. 3.2.3. Contributions to Sections 4, 5, 7, 8. YT, HS: Responsible for Sect. 4. Contributions to Sects. 4, 6, 7, 8. SNJ, SHH: Responsible for Sect. 8. Contributions to Sects. 7, 8. D-HK, HJK: Contributions to Sects. 5, 6, 7, 8. GB, RS: Responsible for Sect. 6. Contributions to Sects. 4, 6, 7. All: Contributions to References sections.

**Funding** Open-access funding was enabled and organized by Project DEAL. The work was conducted by institutional funding and by the following resources. The work at Konkuk University was supported by the National Research Foundation of Korea (NRF) grant by the Korean Government (MSIT), Republic of Korea (2022R1A4A1018884). The work at KARI has been supported by the Korea Aerospace Research Institute's R&D program funded by the Korean Government (MSIT), Republic of Korea (FR22E03; FR23D03). The work in the USA is supported by the US Army DEVCOM AvMC and the NASA Revolutionary Vertical Lift Technology (RVLT) Project. The financial support to Rinaldo Steininger by the Defense Science and Technology Laboratory (DSTL) of the UK is gratefully acknowledged. A part of the results of UofG were obtained using the ARCHIE-WeSt High-Performance Computer ([www.archie-west.ac.uk](http://www.archie-west.ac.uk)), EPSRC grant no. EP/K000586/1.

## Declarations

**Conflict of interest** The authors have no competing interests to declare that are relevant to the content of this article.

**Open Access** This article is licensed under a Creative Commons Attribution 4.0 International License, which permits use, sharing, adaptation, distribution and reproduction in any medium or format, as long as you give appropriate credit to the original author(s) and the source, provide a link to the Creative Commons licence, and indicate if changes were made. The images or other third party material in this article are included in the article's Creative Commons licence, unless indicated otherwise in a credit line to the material. If material is not included in the article's Creative Commons licence and your intended use is not permitted by statutory regulation or exceeds the permitted use, you will need to obtain permission directly from the copyright holder. To view a copy of this licence, visit <http://creativecommons.org/licenses/by/4.0/>.

## References

- Kessler, C.: Active rotor control for helicopters: motivation and survey on higher harmonic control. *CEAS Aeronaut. J.* **1**(1–4), 3–22 (2011)
- Kessler, C.: Active rotor control for helicopters: individual blade control and washplateless rotor designs. *CEAS Aeronaut. J.* **1**(1–4), 23–54 (2011)
- Küfmann, P., Bartels, R., van der Wall, B.G., Schneider, O., Holthusen, H., Gomes, J.: The first wind tunnel test of the DLR's multiple washplate system: test procedure and preliminary results. *J. Am. Helicopter Soc.* **62**(4), 042002–1–13 (2017)
- Küfmann, P.M., Bartels, R., van der Wall, B.G., Schneider, O., Holthusen, H., Postma, J.: The second wind-tunnel test of DLR's multiple washplate system—IBC on a five-bladed rotor with fuselage-mounted (fixed frame) actuators. *CEAS Aeronaut. J.* **10**(2), 385–402 (2019)
- Loewy, R.G.: Recent developments in smart structures with aeronautical applications. *Smart Mater. Struct.* **6**(5), R11–R42 (1997)
- Chopra, I.: Review of state of art of smart structures and integrated systems. *AIAA J.* **40**(11), 2145–2187 (2002)
- Wilkie, W.K., Wilbur, M.L., Mirick, P.H., Cesnik, C.E.S., Shin, S.J.: Aeroelastic analysis of the NASA/army/MIT active twist rotor. In: American Helicopter Society 55th Annual Forum, Montréal, Canada, May 25–27 (1999)
- Cesnik, C.E.S., Shin, S.J., Wilkie, W.K., Wilbur, M.L., Mirick, P.H.: Modeling, design, and testing of the NASA/Army/MIT active twist rotor prototype blade. In: American Helicopter Society 55th Annual Forum, Montréal, Canada, May 25–27 (1999)
- Wilbur, M.L., Yeager, Jr. W.T., Wilkie, W.K., Cesnik, C.E.S., Shin, S.J.: Hover testing of the NASA/Army/MIT active twist rotor prototype blade. In: American Helicopter Society 56th Annual Forum, Virginia Beach, VA, May 2–4 (2000)
- Wilbur, M.L., Mirick, P.H., Yeager, W.T., Jr., Langston, C.W., Cesnik, C.E.S., Shin, S.J.: Vibratory loads reduction testing of the NASA/Army/MIT active twist rotor. *J. Am. Helicopter Soc.* **47**(2), 123–133 (2002)
- Wilbur, M.L., Yeager, Jr. W.T., Sekula, M.K.: Further examination of the vibratory loads reduction results from the NASA/Army/MIT active twist rotor test. In: American Helicopter Society 58th Annual Forum, Montréal, Canada, June 11–13 (2002)
- Shin, S.J., Cesnik, C.E.S., Hall, S.R.: Closed-loop control test of the NASA/army/MIT active twist rotor for vibration reduction. In: American Helicopter Society 59th Annual Forum, Phoenix, AZ, May 6–8 (2003)
- Bernhard, A.P.F., Wong, J.: Wind-tunnel evaluation of a sikorsky active rotor controller implemented on the NASA/Army/MIT active twist rotor. *J. Am. Helicopter Soc.* **50**(1), 65–81 (2005)
- Shin, S.J., Cesnik, C.E.S., Hall, S.R.: Closed-loop control test of the NASA/Army/MIT active twist rotor for vibration reduction. *J. Am. Helicopter Soc.* **50**(2), 178–194 (2005)
- Büter, A., Breitbach, E.: Adaptive blade twist—calculations and experimental results. *Aerosp. Sci. Technol.* **4**(5), 309–319 (2000)
- Wierach, P., Riemenschneider, J., Opitz, S., Hoffmann, F.: Experimental investigation of an active twist model rotor blade under centrifugal loads. In: 33rd European Rotorcraft Forum, Kazan, Russia, Sept. 11–13 (2007)
- Wierach, P., Riemenschneider, J., Opitz, S., Hoffmann, F.: Experimental investigation of an active twist model rotor blade under centrifugal loads, Chapter 32: 391–407. In: Wiedemann, Sinapius (Eds.) *Research Topics in Aerospace: Adaptive, Tolerant and Efficient Composite Structures*, pp. 391–407. Springer, Berlin (2013)
- Riemenschneider, J., Keimer, R., Kalow, S.: Experimental bench testing of an active-twist rotor. In: 39th European Rotorcraft Forum, Moscow, Russia, Sept. 3–5 (2013)
- Hoffmann, F., Schneider, O., van der Wall, B.G., Keimer, R., Kalow, S., Bauknecht, A., Ewers, B., Pengel, K., Feenstra, G.: STAR Hovering test—proof of functionality and representative results. In: 40th European Rotorcraft Forum, Southampton, UK, Sept. 2–4 (2014)
- Lim, J.W., Boyd, Jr. D.D., Hoffmann, F., van der Wall, B.G., Kim, D.-H., Jung, S.N., Tanabe, Y., Bailly, J., Lienard, C., Delrieux, Y.: Aeromechanical evaluation of smart-twisting active rotor. In: 40th European Rotorcraft Forum, Southampton, UK, Sept. 2–4 (2014)
- Bauknecht, A., Ewers, B., Schneider, O., Raffel, M.: Aerodynamic results from the STAR hover test: an examination of active twist actuation. In: 41st European Rotorcraft Forum, Munich, Germany, Sept. 1–3 (2015)
- Hoffmann, F., Keimer, R., Riemenschneider, J.: Structural modeling and validation of an active twist model rotor blade. *CEAS Aeronaut. J.* **7**(1), 43–55 (2016)
- Kalow, S., van de Kamp, B., Keimer, R., Riemenschneider, J.: Experimental investigation and validation of structural properties of a new design for active twist rotor blades. In: 43rd European Rotorcraft Forum, Milan, Italy, Sept. 12–15 (2017)
- Kalow, S., van de Kamp, B., Balzarek, C., Riemenschneider, J.: Manufacturing of a next generation active twist helicopter rotor blade and experimental results of functionality test. In: American Helicopter Society 74th Annual Forum, Phoenix, Arizona, May 14–17 (2018)
- Kalow, S., van de Kamp, B., Keimer, R., Riemenschneider, J.: Next generation active twist helicopter rotor blade—simulated results validated by experimental investigation. In: 45th European Rotorcraft Forum, Warsaw, Poland, Sept. 17–20 (2019)
- Crews, S.T., Hamilton, B.W.: Army helicopter crew seat vibration—past performance, future requirements. In: American Helicopter Society North East Region National Specialists' Meeting on Helicopter Vibration, Hartford, CT, Nov. 2–4 (1981)
- van der Wall, B.G.: Analytic formulation of unsteady profile aerodynamics and its application to simulation of rotors, ESA-TT-1244 (1992, Translation of the Research Report DLR-FB 90–28) (1990)
- van der Wall, B.G., Lim, J.W., Smith, M.J., Jung, S.N., Bailly, J., Baeder, J.D., Boyd, D.D.: The HART II international workshop: an assessment of the state-of-the-art in comprehensive code prediction. *CEAS Aeronaut. J.* **4**(3), 223–252 (2013)
- Houbolt, J.C., Brooks, G.W.: Differential equations of motion for combined flapwise bending, chordwise bending, and torsion of twisted nonuniform rotor blades. *NACA TN 3905* (1957)

30. Leiss, U.: A Consistent mathematical model to simulate steady and unsteady rotor–blade aerodynamics. In: 10th European Rotorcraft Forum, The Hague, Netherlands, Aug. 28–31 (1984)
31. Mangler, K.W., Squire, H.B.: The induced velocity field of a rotor, ARC R&M 2642 (1950)
32. Beddoes, T.S.: A wake model for high resolution airloads. In: American Helicopter Society/ARO 1st International Conference on Rotorcraft Basic Research, Research Triangle Park, North Carolina, Feb. 19–21 (1985)
33. Yin, J., Delfs, J.: Improvement of DLR rotor aero–acoustic code (APSIM) and its validation with analytic solution. In: 29th European Rotorcraft Forum, Friedrichshafen, Germany, Sept. 16–18 (2003)
34. Farassat, F.: Derivation of formulation 1 and 1A of farassat, NASA TM–2007–214853 (2007)
35. Raddatz, J., Fassbender, J.K.: Block structured Navier–Stokes Solver FLOWer. In: Kroll, Fassbender (Eds.) Notes on Numerical Fluid Mechanics and Multidisciplinary Design: MEGAFLOW—Numerical Flow Simulation for Aircraft Design, vol. 89, pp. 27–44, Springer, Berlin–Heidelberg (2005)
36. Benoit, B., Dequin, A.M., Kampa, K., von Grünhagen, W., Basset, P.M., Gimonet, B.: HOST, a general helicopter simulation tool for Germany and France. In: American Helicopter Society 56th Annual Forum, Virginia Beach, VA, May 2–4 (2000)
37. Potsdam, M., Yeo, H., Johnson, W.: Rotor airloads prediction using loose aerodynamic/structural coupling. *AIAA J. Aircraft* **43**(3), 732–742 (2006)
38. Datta, A., Sitaraman, J., Chopra, I., Baeder, J.D.: CFD/CSD Prediction of rotor vibratory loads in high-speed Flight. *AIAA J. Aircraft* **43**(6), 1698–1709 (2006)
39. Wilke, G.: Comparisons of different spatial schemes and limiters for helicopter flows. In: Dillmann et al (Eds.) Notes on Numerical Fluid Mechanics and Multidisciplinary Design: New Results in Numerical and Experimental Fluid Mechanics XIII: Contributions of the 22nd STAB/DGLR Symposium, vol. 151, pp. 418–427, Springer, Berlin (2021)
40. Shur, M.L., Spalart, P.R., Strelets, M.K., Travin, A.K.: A Hybrid RANS–LES Approach with delayed–ES and wall-modelled LES capabilities. *Int. J. Heat Fluid Flow* **29**(6), 1638–1649 (2008)
41. Dacles-Mariani, J., Kwak, D., Zilliac, G.: On numerical errors and turbulence modeling in tip vortex flow prediction. *Int. J. Numer. Methods Fluids* **30**(1), 65–82 (1999)
42. Heister, C.C.: A method for approximate prediction of laminar-turbulent transition on helicopter rotors. *J. Am. Helicopter Soc.* **63**(3), 1–14 (2018)
43. Basset, P.M., Heuze, O., Prasad, J.V.R., Hamers, M.: Finite state rotor induced flow model for interferences and ground effect. In: American Helicopter Society 57th Annual Forum, Washington DC, May 9–11 (2001)
44. Arnaud, G., Beaumier, P.: Validation of R85/METAR on the puma RAE flight tests. In: 18th European Rotorcraft Forum, Avignon, France, Sept. 15–18 (1992)
45. Rodriguez, B.: Blade vortex interaction and vortex ring state captured by a fully time marching unsteady wake model coupled with a comprehensive dynamics code. In: Heli Japan, Saitama, Japan, Nov. 1–3 (2010)
46. Michéa, B., Desopper, A., Costes, M.: Aerodynamic rotor loads prediction method with free–wake for low speed descent flight. In: 18th European Rotorcraft Forum, Avignon, France, Sept. 15–18 (1992)
47. Rahier, G., Delrieux, Y.: Improvement of helicopter rotor blade–vortex interaction noise prediction using a rotor wake roll–up model. In: 1st Joint CEAS/AIAA Aeroacoustics Conference (16th AIAA Aeroacoustics Conference), Munich, Germany, June 12–15 (1995)
48. Spiegel, P., Rahier, G., Michéa, B.: Blade vortex interaction noise: prediction and comparison with flight and wind tunnel tests. In: 18th European Rotorcraft Forum, Avignon, France, Sept. 15–18 (1992)
49. Spiegel, P., Rahier, G.: Theoretical study and prediction of BVI noise including close interactions. In: American Helicopter Society Technical Specialists Meeting on Rotorcraft Acoustics and Fluid Mechanics, Valley Forge, Philadelphia, PA, Oct. 15–17 (1991)
50. Johnson, W.: Rotorcraft aerodynamic models for a comprehensive analysis. In: American Helicopter Society 54th Annual Forum, Washington, DC, May 20–22 (1998)
51. Lopes, L., Burley, C.L.: Design of the next generation aircraft noise prediction program: ANOPP2. In: 17th AIAA/CEAS Aeroacoustics Conference (32nd AIAA Aeroacoustics Conference), Paper AIAA 2011–2854, Portland, OR, June 5–8 (2011)
52. Lee, H., Yu, D., Kwon, O.J., Kang, H.J.: Numerical investigation about aerodynamic interference of complete helicopter configurations. *Int. J. Aeronaut. Sp. Sci* **12**(2), 190–199 (2011)
53. Tanabe, Y., Saito, S., Sugawara, H.: Construction and validation of an analysis tool chain for rotorcraft active noise reduction. In: 38th European Rotorcraft Forum, Amsterdam, Netherlands, Sept. 4–7 (2012)
54. Langtry, R.B., Menter, F.R.: Correlation-based transition modeling for unstructured parallelized computational fluid dynamics codes. *AIAA J.* **47**(12), 2894–2906 (2009)
55. Steijl, R., Barakos, G.N., Badcock, K.: A framework for CFD analysis of helicopter rotors in hover and forward flight. *Int. J. Numer. Meth. Fluids* **51**(8), 819–847 (2006)
56. Osher, S., Chakravarthy, S.: Upwind schemes and boundary conditions with applications to Euler equations in general geometries. *J. Comput. Phys.* **50**(3), 447–481 (1983)
57. van Leer, B.: Towards the ultimate conservative difference scheme. V. A second-order sequel to Godunov’s method. *J. Comput. Phys.* **32**(1), 101–136 (1979)
58. van Albada, G.D., van Leer, B., Roberts, W.W.: A comparative study of computational methods in cosmic gas dynamics. *Astron. Astrophys.* **108**(1), 76–84 (1982)
59. Jameson, A.: Time-dependent calculations using multigrid, with applications to unsteady flows past airfoils and wings. In: AIAA 10th Computational Fluid Dynamics Conference, Honolulu, HI, June 24–26 (1991)
60. Axelsson, O.: *Iterative Solution Methods*. Cambridge University Press, Cambridge (1994)
61. Menter, F.R.: Two-equation Eddy-viscosity turbulence models for engineering applications. *AIAA J.* **32**(8), 1598–1605 (1994)
62. Dehaeze, F., Barakos, G.N.: Hovering rotor computations using an aeroelastic blade model. *Aeronaut. J.* **116**(1180), 621–649 (2012)
63. Smith, M.J., Gardner, A.D., Jain, R., Peters, D., Richez, F.: Rotating wing dynamic stall: state of the art and future directions. In: Vertical Flight Society 76th Annual Forum, Virtual, Oct. 6–8 (2020)
64. Castells, C., Richez, F., Costes, M.: A numerical analysis of the dynamic stall mechanisms on a helicopter rotor from light to deep stall. *J. Am. Helicopter Soc.* **65**(3), 1–17 (2020)
65. Datta, A., Yeo, H., Norman, T.R.: Experimental investigation and fundamental understanding of a slowed UH-60A rotor at high advance ratios. In: American Helicopter Society 66th Annual Forum, Virginia Beach, VA, May 3–5 (2011)

**Publisher's Note** Springer Nature remains neutral with regard to jurisdictional claims in published maps and institutional affiliations.